Article

Developmental Cell

# Organellar Proteomics and Phospho-Proteomics Reveal Subcellular Reorganization in Diet-Induced Hepatic Steatosis

## Graphical Abstract

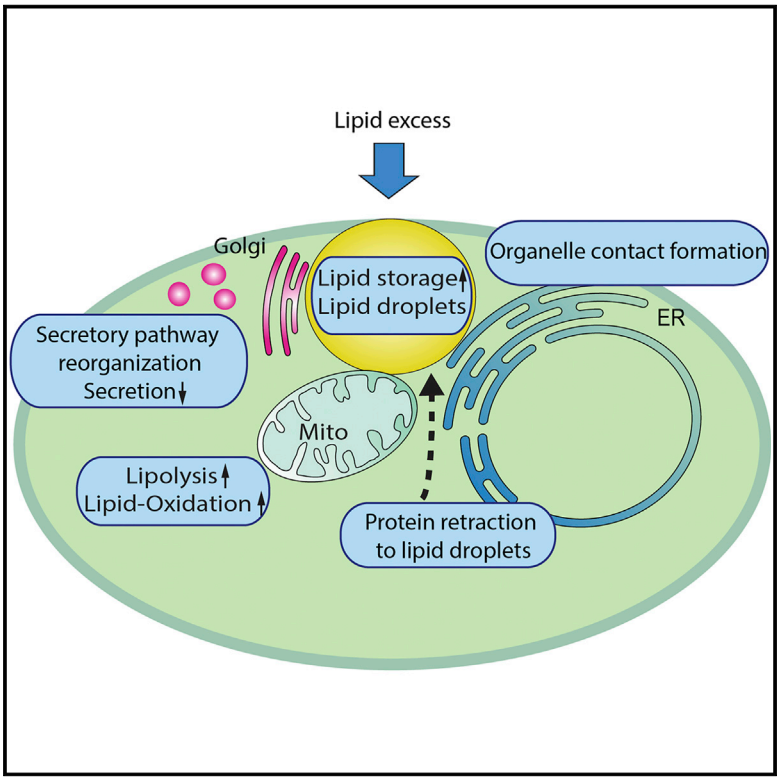


## Highlights

- Protein localization and organelle-specific phosphosites upon hepatic LD accumulation
- HFD induces contacts between organelles, orchestrating lipid metabolism
- LDs sequester compartment-specific proteins upon steatosis
- The secretory apparatus redistributes, reducing protein secretion

## Authors

Natalie Krahmer, Bahar Najafi, Florian Schueder, ..., Anja Zeigerer, Georg Heinz Helmut Borner, Matthias Mann

## Correspondence

mmann@biochem.mpg.de

## In Brief

The systematic proteomic *in vivo* analysis of subcellular rearrangements and organelle-specific phosphorylation by Krahmer et al. reveals how nutrient overload leads to organellar reorganization and cellular dysfunction in NAFLD. Lipid accumulation changes organelle contacts and leads to a dramatic redistribution of secretory pathway proteins, thereby affecting hepatic secretion.

Krahmer et al., 2018, Developmental Cell *47*, 205–221
October 22, 2018 
https://doi.org/10.1016/j.devcel.2018.09.017

CellPress

Developmental Cell
Article

# Organellar Proteomics and Phospho-Proteomics Reveal Subcellular Reorganization in Diet-Induced Hepatic Steatosis

Natalie Krahmer,[1] Bahar Najafi,[2,3,4] Florian Schueder,[5,6] Fabiana Quagliarini,[7] Martin Steger,[1] Susanne Seitz,[2,3,4] Robert Kasper,[8] Favio Salinas,[9] Jürgen Cox,[9] Nina Henriette Uhlenhaut,[7] Tobias Christian Walther,[10,11,12,13] Ralf Jungmann,[5,6] Anja Zeigerer,[2,3,4] Georg Heinz Helmut Borner,[1] and Matthias Mann[1,14,15,*]
[1]Proteomics and Signal Transduction, Max-Planck Institute of Biochemistry, Martinsried 82152, Germany
[2]Institute for Diabetes and Cancer, Helmholtz Center Munich, Neuherberg 85764, Germany
[3]Joint Heidelberg-IDC Translational Diabetes Program, Inner Medicine 1, Heidelberg University Hospital, Heidelberg, Germany
[4]German Center for Diabetes Research (DZD), Neuherberg 85764, Germany
[5]Department of Physics and Center for Nanoscience, Ludwig Maximilian University, Munich, Germany
[6]Max Planck Institute of Biochemistry, Martinsried 82152, Germany
[7]Helmholtz Diabetes Center (HMGU) and German Center for Diabetes Research (DZD), IDO, Garching, Munich 85748, Germany
[8]Max Planck Institute of Neurobiology, Imaging facility, Martinsried 82152, Germany
[9]Computational Systems Biochemistry, Max-Planck Institute of Biochemistry, Martinsried 82152, Germany
[10]Department of Genetics and Complex Diseases, Harvard T.H. Chan School of Public Health, Boston, MA 02115, USA
[11]Department of Cell Biology, Harvard Medical School, Boston, MA 02115, USA
[12]Broad Institute of Harvard and MIT, Cambridge, MA 02142, USA
[13]Howard Hughes Medical Institute, Boston, MA 02115, USA
[14]Faculty of Health Sciences, NNF Center for Protein Research, University of Copenhagen, Copenhagen 2200, Denmark
[15]Lead Contact
*Correspondence: mmann@biochem.mpg.de
https://doi.org/10.1016/j.devcel.2018.09.017

## SUMMARY

**Lipid metabolism is highly compartmentalized between cellular organelles that dynamically adapt their compositions and interactions in response to metabolic challenges. Here, we investigate how diet-induced hepatic lipid accumulation, observed in non-alcoholic fatty liver disease (NAFLD), affects protein localization, organelle organization, and protein phosphorylation *in vivo*. We develop a mass spectrometric workflow for protein and phosphopeptide correlation profiling to monitor levels and cellular distributions of ~6,000 liver proteins and ~16,000 phosphopeptides during development of steatosis. Several organelle contact site proteins are targeted to lipid droplets (LDs) in steatotic liver, tethering organelles orchestrating lipid metabolism. Proteins of the secretory pathway dramatically redistribute, including the mis-localization of the COPI complex and sequestration of the Golgi apparatus at LDs. This correlates with reduced hepatic protein secretion. Our systematic *in vivo* analysis of subcellular rearrangements and organelle-specific phosphorylation reveals how nutrient overload leads to organellar reorganization and cellular dysfunction.**

## INTRODUCTION

Lipid metabolism involves many functionally distinctive cellular organelles, which provide separate compartments for their diverse biochemical reactions. These compartments are highly dynamic structures that change both their composition and interactions to adapt to environmental changes and metabolic challenges. For example, lipid uptake, synthesis, storage, and degradation involve the plasma membrane, ER, mitochondria, peroxisomes, lysosomes and, in addition, lipid droplets (LDs). LDs are storage organelles that function in the core of lipid metabolism and mediate many metabolic processes, including neutral lipid synthesis and mobilization. To orchestrate lipid metabolism and enable substrate flux, they form membrane bridges with the ER and interact with many other organelles, such as mitochondria (Gao and Goodman, 2015; Wilfling et al., 2013).

LD accumulation in peripheral organs and overflow of toxic lipid species are the hallmark of obesity-associated diseases, such as type 2 diabetes or cardiovascular diseases (Krahmer et al., 2013a). In the liver, lipid overflow leads to various pathologies, ranging in severity from mild hepatosteatosis to non-alcoholic steatohepatitis (NASH), which can progress to liver failure (Cohen et al., 2011). Although ER stress and mitochondrial dysfunction have been reported in steatotic liver (Biddinger et al., 2008), it is still not clear how extensive lipid accumulation affects protein localization, organelle architecture, and interactions. Specifically, protein composition is a key factor controlling organelle functions and is determined by different mechanisms such as protein-protein interactions or post-translational modifications (PTMs), especially phosphorylation (Bauer et al., 2015). Understanding how hepatic lipid accumulation affects the organelle protein composition and their PTM therefore has a broad impact on metabolism in health and disease.

Determining organelle composition, protein localization, and the phosphorylation status of proteins in the native environment

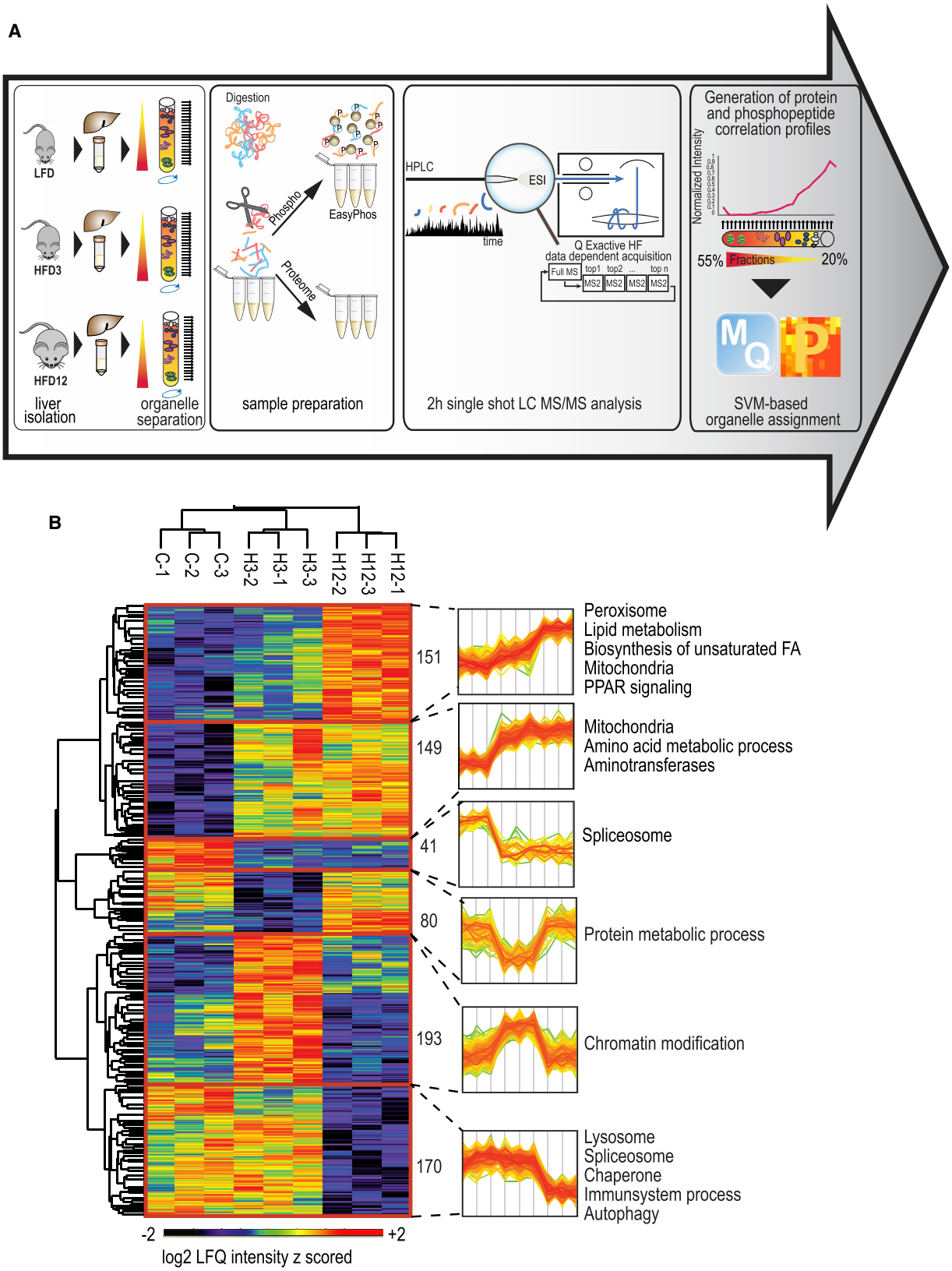


(legend on next page)

of cells and under pathological conditions is challenging with conventional cell biological methods, especially in a high-throughput manner, as protein localization is difficult to assess in organs. Many antibody-based methods are impractical at a large scale due to antibody availability, especially of those that allow immunofluorescence in tissue or the detection of PTMs. As a consequence, many studies have used cell line models, but these do not necessarily reflect the *in vivo* situation, where cells are exposed to different stimuli such as metabolic hormones secreted into the bloodstream from different organs.

Here, we set out to address the effect of lipid overload on the cellular organization by analyzing changes in protein localization and phosphorylation in a mouse model for hepatic steatosis using an unbiased approach. Recently, the development of novel technologies has advanced organellar proteomics. For instance, proximity labeling strategies such as APEX allow the proteomic analysis of organelles such as LDs that are hard to purify to complete homogeneity (Bersuker et al., 2018), whereas subcellular fractionation coupled to mass spectrometry (MS)-based methods has facilitated the global analysis of cellular organization. Systematic profiling approaches, such as "protein correlation profiling" (PCP) (Andersen et al., 2003; Foster et al., 2006), localization of organelle proteins by isotope tagging (LOPIT) (Christoforou et al., 2016), and organellar maps (Itzhak et al., 2016) have been used to determine organellar composition and dynamics in an unbiased manner. The principle of PCP as well as related technologies is that the majority of proteins are quantified in many or all fractions of the gradient. This is enabled by the high sensitivity and coverage of modern proteomics methods and—far from being problematic—is the basis of organelle assignment through localization profiles, rather than presence or absence in single fractions. In this way, protein and phosphopeptide correlation profiling is based on the generation of characteristic profiles over the complete purification gradients and therefore allows the determination of protein and phosphopeptide localization without purification of the organelles to complete homogeneity. PCP has already proven to be useful in the extensive characterization of the LD proteome (Krahmer et al., 2013b).

In some cases, protein phosphorylation promotes or correlates with its relocalization. But these events are not available in either organellar maps or large-scale phosphoproteomic data acquired so far. To generate data required for this integration, we combined PCP with a recently developed phosphoproteomic protocol termed EasyPhos, which enables in-depth phosphoproteome analyses from minimal amounts of protein material, such as organelle fractions in a high-throughput manner (Humphrey et al., 2015).

This workflow allowed us to map organelle-specific phosphorylation and to determine changes in subcellular protein distribution during the development of hepatic steatosis. We identified hundreds of proteins with changes in subcellular localization and discovered organelle-specific protein phosphorylation changes that correlate with protein relocalization. Our data revealed drastic organellar reorganization upon LD accumulation during the development of steatosis.

## RESULTS

### Metabolic Reprogramming during HFD

To induce hepatosteatosis, we fed mice a high-fat diet (HFD) for either 3 weeks (early time point) or 12 weeks (late time point), whereas a control group was kept on a low-fat diet (LFD). All mice were sacrificed in an ad libitum-fed state at the age of 16 weeks. After 3 weeks, mice were insulin resistant as measured by an oral glucose tolerance test (OGTT) (Figures S1A and S1B), whereas hepatic triglyceride (TG) levels were not significantly altered. After 12 weeks of HFD, fatty liver had developed with an almost 300% increase in TGs (Figure S1C). We analyzed the total proteome, the total phosphoproteome, and the organelle-resolved proteome and phosphoproteome in these mice (Figure 1A).

First, to test the influence of HFD on protein levels, we characterized the temporal changes in the liver proteome. We identified 7,394 proteins (Figure S1D). The Pearson correlation between biological replicates was on average 0.98. Replicates of the same time points clustered together in a principal-component analysis (PCA) (Figure S1E). In a stringently filtered dataset of 6,112 proteins quantified at least once in two or more biological replicates of one time point, more than 12% (784) of the proteins were differentially regulated in response to HFD (ANOVA; false discovery rate (FDR) 0.05). Of the changed proteins, 53% are Gene Ontology (GO)-annotated as involved in cellular metabolic processes. While statistically significant, the changes in the levels of metabolic enzymes were, in general, moderate (1.2- to 2-fold) (Figure S1F).

Hepatocytes responded to lipid oversupply with a gradual increase in peroxisomal and mitochondrial fatty acid (FA) utilization (GO terms: beta-oxidation, TCA cycle, oxidative phosphorylation, and ketone body metabolism) and with promoting lipid synthesis and storage (lipid biosynthetic process, cholesterol biosynthesis, biosynthesis of FAs, and lipid transport) (Figures 1B and S1G). For instance, levels of CD36 and FABP2, proteins involved in the transport of FAs, increased 1.8- and 2.3-fold, respectively. The abundance of main organizers and enzymes of TG storage in LDs such as PLIN2 or ACSL1 increased 2.7- and 1.5-fold, respectively, and levels of several apolipoproteins were augmented. Providing a positive control, PPARα targets were specifically enriched among proteins with increased levels ($p < 2.95E{-}05$), indicating an activation of PPARα signaling and induction of peroxisomal proliferation (Figures 1B and S1G). For complete proteomic data, fold

**Figure 1. Proteomic Changes Leading to Metabolic Reprogramming during HFD**

(A) Experimental design of the study. For each experimental group, the total liver proteome and phosphoproteome were determined and organelles characterized by protein and phosphopeptide correlation profiling.

(B) Proteomic changes during HFD. Hierarchical clustering of label-free quantitation (LFQ) intensities of 787 significantly changed proteins (ANOVA, FDR 0.05) in the total proteome revealed clusters of a temporal response to HFD. Numbers of proteins, intensity profiles, and selected enriched GO terms, KEGG pathways, and keywords (Fisher's exact test, FDR 0.1) with their enrichment factors are indicated for marked clusters.

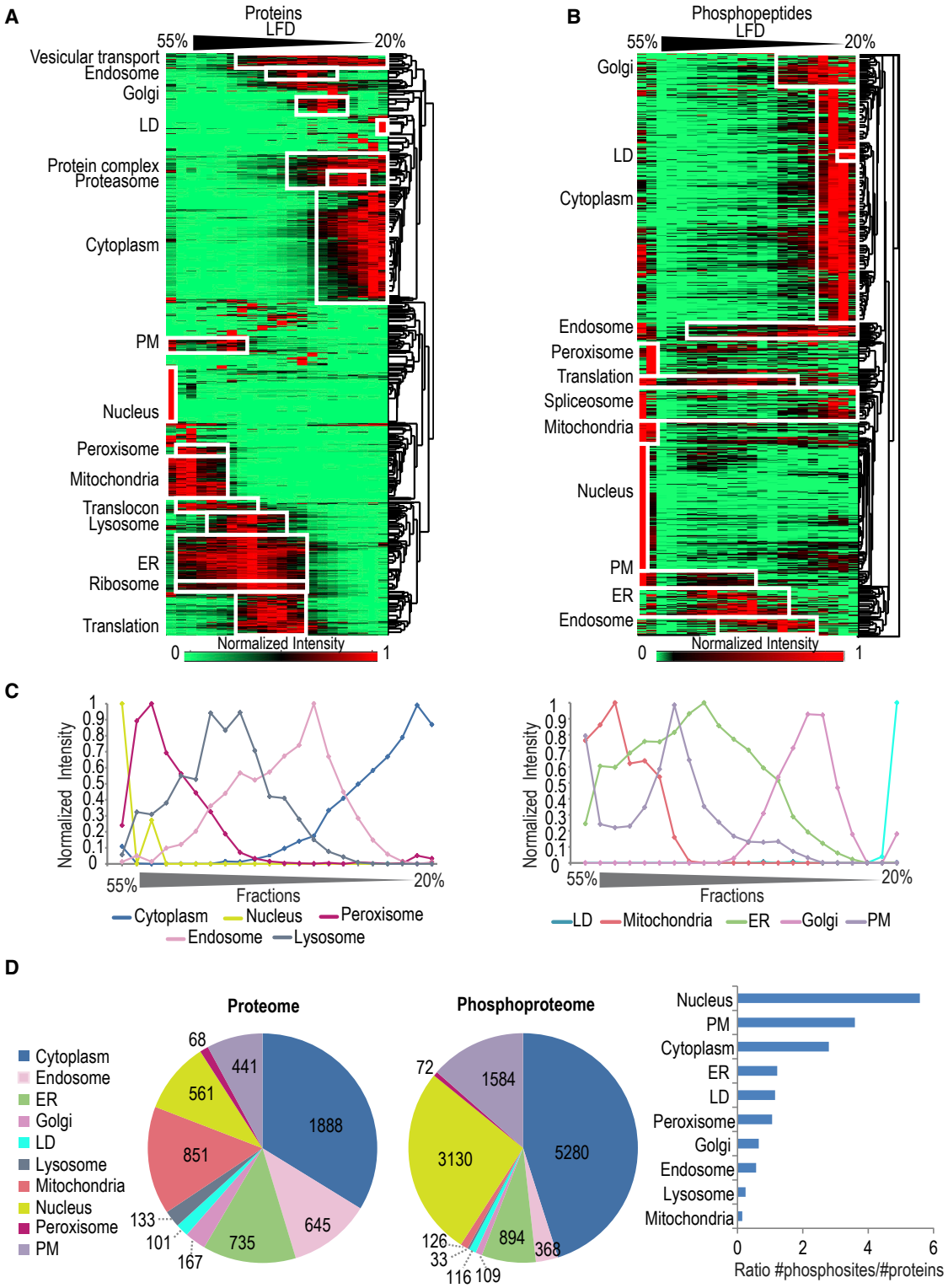


**Figure 2. Characterization of Subcellular Organelle Proteomes and Organelle-Specific Phosphorylation in the Mouse Liver**

(A) Hierarchical clustering of protein profiles (5,812 median profiles of three biological replicates of the LFD control group for proteins identified in all three replicates) demonstrating separation of subcellular organelles and protein complexes by correlation profiling. Enriched organelles and protein complexes are indicated.

(B) Hierarchical clustering of phosphopeptide profiles (13,686 median profiles of four biological replicates of the LFD control group, filtered for sites that were quantified in at least three of the four replicates). Enriched organelles and protein complexes are indicated.

*(legend continued on next page)*

changes of all quantified proteins and complete 1D annotation enrichment, see Table S1.

Besides upregulation of lipid storage and utilization pathways, HFD had a strong impact on amino acid metabolism. We found increased levels of enzymes involved in branched chain amino acid degradation (Figure S1G), as previously described (Guo et al., 2013).

Interestingly, the abundance of most quantified lysosomal hydrolases was 2- to 4-fold decreased at the late time point of HFD (Figure 1B). This could be due to an inactivation of autophagy after longer periods of lipid exposure (Papáčková et al., 2012). Consistent with this notion, several positive regulators of autophagosome formation were also detected at lower levels at this time point (Figure 1B).

In addition, the abundance of many nuclear factors regulating chromatin organization, transcription, mRNA processing, and proteins involved in translation were reduced under HFD, generally to a modest degree (1.5 to 3-fold). For instance, the transcription factor STAT3 was reduced 1.5-fold, and the transcription coactivator CREBBP was reduced 3.5-fold. Thus, our total proteome results indicate that HFD influences protein expression and degradation, as also proteasomal components were upregulated (2- to 6-fold) (Figures 1B and S1G).

For the analysis of the total liver phosphoproteome, we filtered phosphopeptides for at least two valid values among three biological replicates in at least one condition. To account for the strong changes on the proteome level under HFD, we first normalized phosphopeptide levels to protein levels. Phosphopeptides without protein information were discarded from the analysis. This resulted in a dataset of 10,084 phosphopeptides, of which 2,302 were significantly increased or decreased (Table S2). The increased phosphosites were enriched in kinase motifs for PKC and specifically the atypical family member PKCε (Figure S1H). This is interesting because these kinases are activated by increased cellular lipid levels such as diacylglycerols, and PKCε is thought to play an important role in the development of hepatic insulin resistance (Petersen et al., 2016). An upregulation of PKCε activity under HFD was supported by the finding that the phosphorylated form of the S729 peptide was only detectable in the HFD condition, as revealed by the total phosphoproteome, whereas its total protein levels remained constant (Figure S1I). S729 autophosphorylation is required for kinase activation and indicates its activity (Newton and Messing, 2010). At the same time, substrate motifs for casein kinase II and ATM kinase, which are regulated by insulin levels (Yang and Kastan, 2000), were enriched among downregulated phosphorylation sites under HFD (Figure S1H).

## Characterization of Subcellular Organelle Proteomes and Phosphoproteomes in the Mouse Liver

To characterize HFD-induced changes in organelle composition, we adapted PCP, a proteomic method for unbiased assignment of proteins to multiple subcellular localizations (Andersen et al., 2003). Briefly, we separated cellular organelles on a sucrose density gradient, determined the composition of the organelle-enriched fractions by proteomics, and used our EasyPhos workflow for the analysis of the organelle phosphoproteomes (Humphrey et al., 2015). Raw MS data were analyzed in the MaxQuant environment for accurate peptide and protein identification, label-free quantification, and phosphosite localization. We derived protein and phosphopeptide profiles from the analyzed organelle fractions by scaling intensities for each quantified protein or phosphopeptide over all fractions of the purification procedure to a value of 0 to 1, after normalizing protein and phosphopeptide levels to the same protein input (Figure 1A).

Hierarchical clustering of protein and phosphopeptide profiles of the control mice (LFD) showed that major organelles and large protein complexes were well separated (Figures 2A and 2B). For each organelle, we determined the median profile of a set of specific markers (Figures 2C and S2A). The fractionation procedure was highly reproducible, as the median Pearson correlation for profiles of the same protein was 0.87 among biological replicates. Median protein and phosphopeptide organelle marker profiles from biological replicates were highly similarly distributed (Figures S2B and S2C), allowing label-free comparison of different biological conditions. These profiles had characteristic shapes for the different organelles, demonstrating that proteins and phosphopeptides from the same organelles fractionate similarly (Figures 2C and S2C). Subunits of protein complexes had almost identical profiles (Figures S2D and S2E).

In contrast to the specific organelle markers, most protein profiles and many phosphopeptide profiles reflected a combination of multiple subcellular localizations, in agreement with previous observations from us and others (Foster et al., 2006; Thul et al., 2017). To bioinformatically address this, we developed a workflow combining support vector machines (SVMs) and correlation profiling for the quantitative assignment of the two main organelles (Figure S3A).

We quantified 6,974 proteins in the organellar map, with an average of 3,000–4,000 proteins in each of the organelle fractions (Figure S3B). Of those, we successfully spatially mapped 5,648 proteins in at least one biological condition and 4,456 in all three conditions to 10 different cellular compartments (Figure S3C) (see Table S3 for complete PCP data and for organelle assignments).

Phosphopeptide profiling in an organellar context is challenging due to the limited protein amount in many of the organelle fractions, as well as the high number of fractions. However, our high sensitivity EasyPhos platform allowed us to enrich phosphopeptides in a high-throughput manner for the organelle fractions. Using biological quadruplicates, we compared 176 phosphoproteomes in the LFD condition to the late time point of HFD. In total, we quantified 24,523 phosphosites on 4,151 phosphoproteins. Among the organellar fractions, the number of quantified sites ranged from 4,400 to more than 11,000 (Figure S3D). Altogether, 16,087 phosphopeptides had assignable organellar profiles, with 9,990 of these in both feeding conditions

(C) Median profiles of three biological replicates of marker proteins for the indicated cellular compartments. Characteristic peaks for each organelle or protein complex allow the organelle assignment to each protein profile.

(D) Sizes of organelle proteomes and phosphoproteomes based on the main SVMs' assignments on all fractions, biological replicates, and experimental conditions. The ratio of phosphosites/protein numbers reveals the extent of protein phosphorylation in cellular compartments.

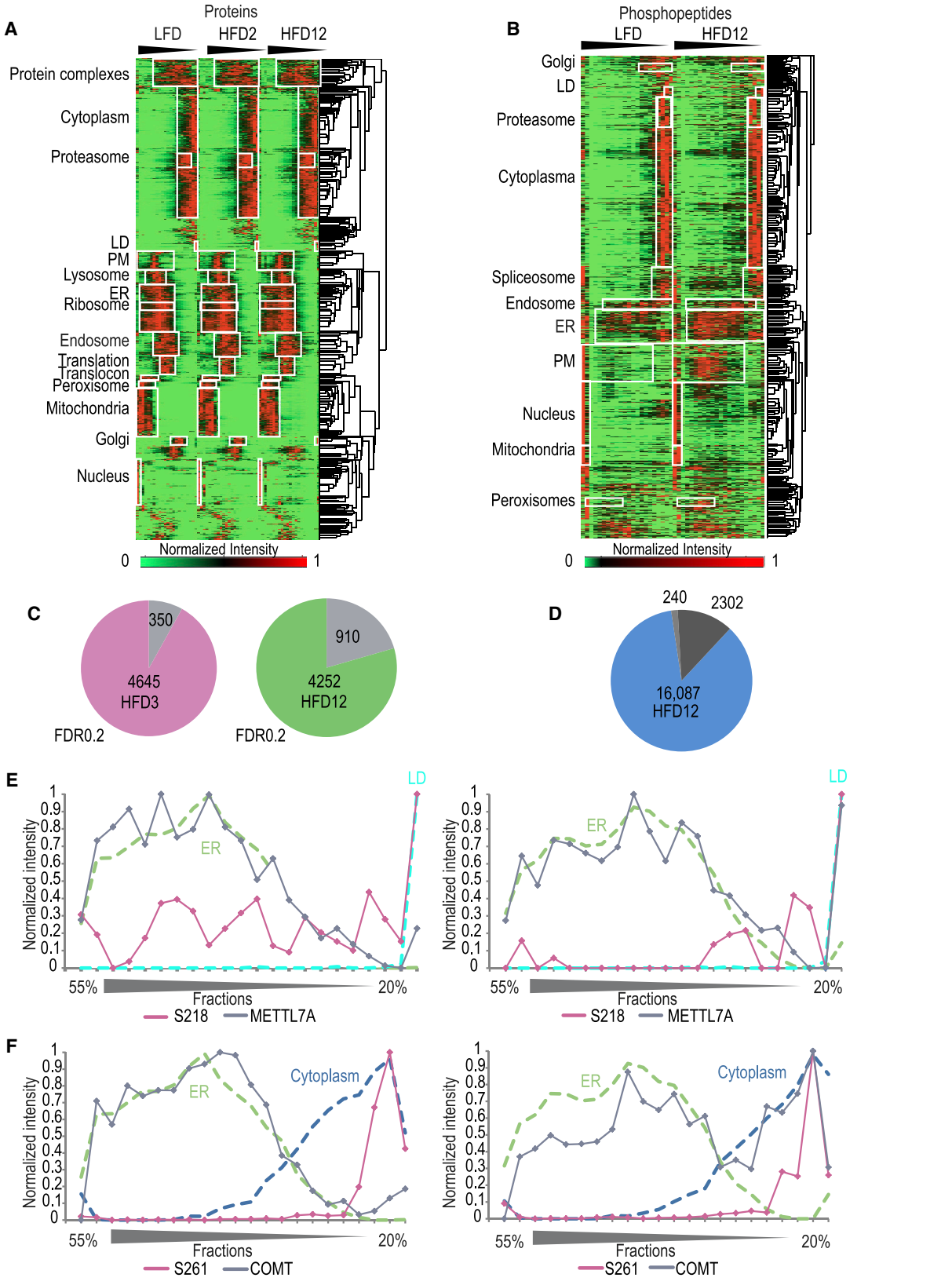


*(legend on next page)*

(Figure S3C) (see Table S4 for complete phosphopeptide correlation profiling data and organelle assignments).

Our organellar proteome and phosphoproteome data show that the extent of protein phosphorylation varies between cellular compartments. Most phosphosites are assigned to the nucleus, plasma membrane, and cytoplasm, whereas they are underrepresented in mitochondria, as predicted before (Humphrey et al., 2013) (Figure 2D). This reflects biological functions, such as the prominence of the plasma membrane in signaling events and the evolutionary history of mitochondria (Gnad et al., 2010).

Our dataset can be used to map organelle-specific phosphorylation by overlaying the protein profiles with the phosphopeptide profiles of the same protein. Phosphopeptide profiles completely overlapped with their corresponding protein profiles in many cases, but interestingly, in a subset, they only peaked in one of the organellar peaks, indicating compartment-specific phosphorylation. Examples for either compartment-specific or independent phosphorylations can be found on the cytoskeletal protein CTTN or the signaling protein GRB7 (Figures S3E and S3F).

## Mapping of Protein Relocalization and Associated Organelle-Specific Phosphorylation

To systematically analyze changes of organelle proteomes and organelle-specific phosphorylation induced by HFD, we compared the protein and phosphopeptide profiles of the control animals (LFD) to HFD mice at an early time point (3 weeks) and when liver steatosis had manifested (12 weeks). Hierarchical clustering of the median protein and phosphopeptide profiles of LFD and HFD conditions in the biological replicates indicate that high intensity peaks of the organelle clusters are highly similar under all three conditions (Figures 3A and 3B). For most of the compartments, the organelle marker profiles are almost identical among the different time points of HFD. To robustly identify the subset of proteins relocalizing in response to lipid overload, we developed a "correlation-based outlier test," which relates the profile correlation within the replicates to those between conditions. Because proteins associated with LDs only occur in the lowest density fraction, we separately quantified this relocalization event. From about 4,500 proteins with at least two highly reproducible profiles between biological replicates for the compared conditions, 350 (7.5%) relocalized at the early time point and 910 at the late time point of HFD (21.5%) (FDR 0.2) (Figure 3C and Table S5). Of these 910 proteins, 30% were sequestered to LDs. Of the 350 proteins significantly shifting their subcellular localization at the early HFD time point, 35% were also relocalizing at the late time point.

We normalized the apparent phosphopeptide changes to the proteome analysis of total liver lysate to directly assess regulation of phosphorylation events. Among the more than 16,000 quantified and mapped phosphorylation sites in the phosphopeptide correlation profiling, 2,302 significantly changed their levels at the late time point of HFD in the total phosphoproteome (Figure 3D and Table S2) (FDR 0.1). 240 of those significantly changed sites were on relocalized proteins and 35% of those on relocalized LD proteins (Figure 3D). Phosphorylation changes on those sites might therefore either induce protein relocalization or be a consequence of the interaction with specific kinases at the new compartment. Indeed, overlaying protein and phosphopeptide profiles revealed organelle-specific phosphorylation in at least half of these cases.

Among the relocalizing proteins with correlating phosphorylation changes, we found an enrichment of cytoskeletal and spliceosomal proteins, plasma membrane, Golgi apparatus, or nuclear proteins in the LFD condition. The same category was enriched for proteins relocalizing to LDs under HFD (Figures S4A and S4B). This highlights the role of those compartments as dynamic hotspots for signaling. Specific kinase substrate motifs for main metabolic kinases, such as AKT, PKA, or PKC, were enriched in the phosphorylation sites of those proteins (Figure S4C). However, these kinase motifs did not show any organelle specificity.

An example of a phosphorylation that correlates with protein relocalization is S218 on METTL7A, a putative methyltransferase shuttling between LDs and the ER (Zehmer et al., 2009). Under HFD, the portion of the protein associated with the ER decreases and LD association increases, as confirmed by immunofluorescence in liver tissue (Figure S4D). While S218 phosphorylation was not even detected in the total phosphoproteome in the LFD condition, there was a strong, LD-specific MS signal for the corresponding phosphopeptide in the steatotic condition, revealing a localization-correlated phosphorylation event (Figure 3E). S218 is located in a region in the protein C terminus highly enriched in PTM sites, indicating that this part of the protein might be accessible and important for protein regulation. Furthermore, phosphorylation at this site is increased in obese mice (Grimsrud et al., 2012). To directly assess whether phosphorylation of S218 is sufficient for LD targeting, we generated a mutant in which S218 is replaced by alanine that cannot be phosphorylated. However, similar to the wild-type form, the mutant localized to LDs immediately upon their formation (Figures S4E and S4F). This indicates that additional PTMs might

**Figure 3. Analysis of Protein Localization and Organelle-Specific Phosphorylation under HFD**

(A) Hierarchical clustering of protein profiles (5,188 median profiles of three biological replicates, filtered for proteins identified in all three conditions) of all biological conditions. Organelles and protein complexes enriched in certain clusters are indicated.

(B) Hierarchical clustering of phosphopeptide profiles (11,533 median profiles of four biological replicates, filtered for phosphopeptides identified in at least three of four biological repplicates and in both conditionds. Organelles and protein complexes enriched in certain clusters are indicated.

(C) Number of proteins with reproducible shifts in their protein profile at either time point of HFD filtered by combining of a "correlation-based outlier test" and a test for relocalized LD proteins (correlation-based outlier test, FDR 0.2).

(D) Among the mapped phosphosites, 1,084 were significantly changed under HFD (Student's t test, FDR 0.1) and 240 of those on relocalized proteins.

(E) Overlay of the profiles of METTL7A and its LD-specific phosphosite S218 with ER and LD organelle marker profiles under LFD and HFD. METTL7A relocalization to LDs under HFD is correlated with an increase in S218 phosphorylation.

(F) Overlay of the profiles of COMT and its cytosol-specific phosphosite S261 with ER and cytoplasm organelle marker profiles under LFD and HFD. The increase of cytosolic COMT under HFD is correlated with an increase in S261 phosphorylation.

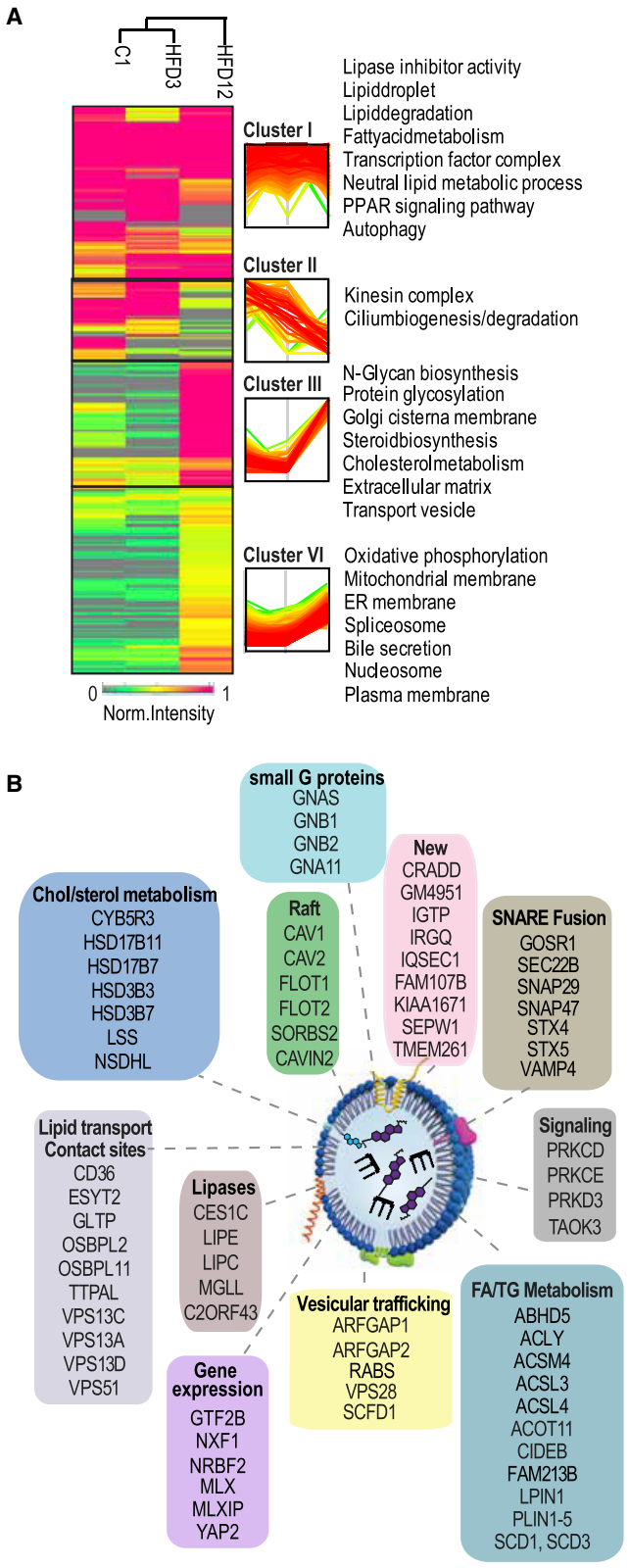


**Figure 4. Changes in the LD Proteome under HFD**

(A) Time-resolved changes of the LD proteome under HFD. Unsupervised hierarchical clustering of protein profile value of the lowest density fraction (FR1) from mean profiles of 1,076 filtered proteins localizing to LDs in at least one condition reveals different LD protein clusters. Proteins in cluster I are present on LDs under all conditions. Cluster II proteins decrease under HFD, and cluster III and IV proteins relocalize partially or completely to LDs under HFD. Selected enriched GO terms, KEGG pathways, and keywords (FDR 0.2) are indicated for each protein cluster.

(B) Functional groups of proteins identified in the LD proteome by protein correlating profiling.

act in concert to determine localization or, alternatively, that S218 phosphorylation might be a consequence of LD targeting by the interaction with kinases after relocalization.

Another interesting compartment-specific phosphorylation site occurs on catechol methyltransferase (COMT), an enzyme involved in the degradation of neurotransmitters, which is also highly expressed in liver. Polymorphisms in COMT are associated with an increased risk of type 2 diabetes (Xiu et al., 2015). COMT has a membrane bound and a cytosolic form that differ by an N-terminally located transmembrane domain. C-terminal S261 phosphorylation was specific to the cytosolic form and strongly increased with elevated cytosolic localization of the enzyme under HFD (Figures 3F and S4G). This site is metabolically regulated and responds to refeeding (Grimsrud et al., 2012). Thus, phosphorylation of this site is likely controlled by compartmentalization.

## Relocalization of Key Signaling and Lipid Metabolism Players during Short-Term HFD

A GO-term analysis did not yield significantly enriched terms among the relocalized proteins at the early time point of HFD, indicating an absence of global effects of protein relocalization. Nevertheless, we observed specific localization changes for several important regulators of cellular signaling pathways such as PRKACA, KRAS, RAF1, GNAS, or ARRB1. Moreover, several proteins organizing the cytoskeleton or involved in vesicular trafficking and lipid metabolism showed significant profile shifts (Figure S4H). For example, serine palmitoyl-CoA transferase SPTLC1, the key enzyme in sphingolipid biosynthesis, relocalized from the ER to the plasma membrane (Figure S4I). Interestingly, the transcription factor TAF15, which controls the expression of a wide range of genes and shuttles between the nucleus and cytosol (Jobert et al., 2009), dramatically shifted toward the nuclear fraction (Figure S4J), which was maintained during the prolonged HFD.

## Long-Term HFD-Induced Changes in the LD Proteome and Formation of Inter-Organelle Contacts

A systematic investigation of changes in the organelle proteomes during HFD (Table S6) indicated that in contrast to the early time point, when steatosis manifests, whole organelle structures and functional protein classes were affected, many of them targeting LDs. To confirm the LD targeting of selected proteins and to verify the accuracy of profiles obtained by data-dependent acquisition (DDA) and label-free quantification, we compared our protein profiles with those generated by a targeted proteomics method: parallel-reaction monitoring (PRM) (Peterson et al., 2012). We targeted three peptides for four LD proteins in the 12-week HFD condition.

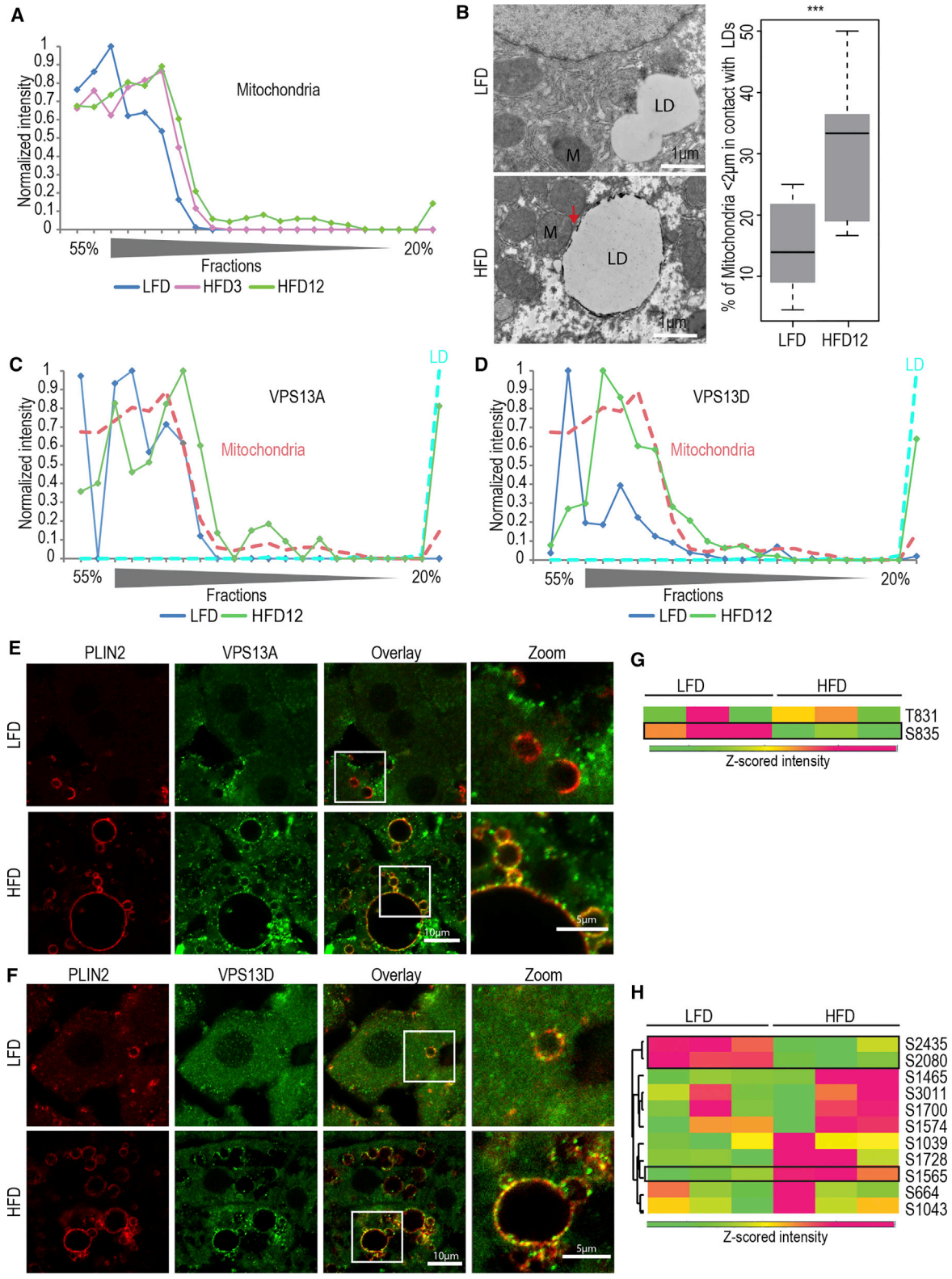


Krahmer et al., Figure 5

*(legend on next page)*

The data reveal a complete overlay of profiles generated by these different MS methods (Figure S5 and Table S7).

To investigate the changes of the LD proteome over the time course of HFD, we defined this subset by filtering for proteins that had their dominant peak in the lowest density fraction, which is characteristic of LD marker proteins. Hierarchical clustering of normalized protein intensities defined four distinct classes of LD proteins diverging in their response to HFD (Figure 4A). Localization of cluster I LD proteins was independent of the diet, and they were detected in the LD fraction under LFD and HFD conditions. This class encompassed canonical LD markers such as PLIN1-5, CIDEB, and HSL and was enriched for TG and FA metabolism categories. Furthermore, it contained several new candidates for cluster I LD proteins such as kinases involved in the development of insulin resistance (PRKCD, PRKCE, and their downstream kinase MEK5), indicating new functions for LDs in the organization or compartmentalization of cellular signaling pathways (Figure 4B). Cluster II proteins were present on LDs under LFD, and their amount decreased during HFD. Many proteins of the cytoskeleton (e.g., kinesin complexes) were found in this category. Cluster III and IV proteins increased their LD localization under HFD. Cluster III is largely composed of proteins annotated as localized in the extracellular matrix, the Golgi apparatus, or involved in vesicular transport. In contrast to cluster III proteins, whose complete cellular pool was targeted to LDs, only a small fraction of the cellular pool of cluster IV proteins co-fractionated with LDs. This suggests that cluster IV proteins either have a dual subcellular localization (such as ER and LD) or localize to organelle membrane domains specifically interacting with LDs and thereby localize to membrane fragments or vesicles that co-purify with LDs. Proteins localizing to the ER membrane, mitochondrial membrane, or plasma membrane were found in this cluster (Table S6). We reasoned that an association between LDs and other organelle membrane regions under HFD would manifest as additional LD-associated pools for membrane proteins from these compartments. Indeed, such pools causing an additional LD peak in the profile clearly appeared for the ER, mitochondria, plasma membrane, and nuclear markers at the late time point of HFD. This suggests the establishment or the strengthening of inter-organelle contacts under a long-term HFD (Figures 5A and S6A–S6C).

To directly test this hypothesis, we imaged mitochondria and LDs by immunofluorescence microscopy in primary hepatocytes derived from LFD- and HFD-fed mice. The mitochondria stained with an antibody for the mitochondrial marker TOM20 were evenly distributed throughout the cells derived from LFD mice but accumulated in regions around LDs in hepatocytes from HFD-mice for 12 weeks (Figure S6D). In addition, ultrastructural analyses by electron tomography revealed a significant increase in the number of mitochondrial-LD contact sites. This increase was not only due to a larger number of LDs in the HFD condition, since the proportion of mitochondria in contact with LDs also increased significantly (Figures 5B and S6E). In the LFD condition, 14% of mitochondria in an area of 2 μm around an LD formed direct contacts, whereas 34% did so under HFD (Student's t test, $p < 0.01$).

Interestingly, our data clearly indicate that several contact site proteins redistribute to LDs at the same time point of HFD when the organelle interactions were detected. For instance, the mitochondrial proteins VPS13 A and D, homologs of the yeast Vps13 protein known to mediate various inter-organelle interactions (Lang et al., 2015), as well as the plasma membrane-ER contact site protein ESYT2 (Saheki et al., 2016), showed partial LD localization after 12 weeks of HFD (Figures 5C, 5D, 5E, 5F, S6F, and S6G). The LD peak under HFD for these contact site proteins was much higher than the median mitochondrial and plasma membrane peak in this fraction, suggesting enrichment in opposed membrane regions.

The formation of contact sites and membrane association of contact sites proteins has recently been shown to be regulated by phosphorylation in some cases (Lees et al., 2017), which prompted us to specifically look for phosphorylation changes correlating with protein relocalization in those proteins. For instance, in VPS13A, relocalization correlated with a decrease in S835 phosphorylation; in VPS13D, with a decrease in S2080 and S2435; and an increase in S1565 phosphorylation (Figures 5G and 5H). Similarly, relocalization of ESYT2 to LDs coincided with almost 9-fold changes of doubly phosphorylated peptides (S683 S685 and S679 S682).

## Long-Term HFD Induces Changes in Golgi Structure and Secretory Function

Bioinformatic analyses demonstrated that specific compartments and functional protein groups were strongly enriched among the relocalized proteins in the steatotic condition, suggesting large-scale reorganization of organellar organization (Figure 6A). "Golgi apparatus" and "Golgi membrane" were the most significant categories in the relocalized proteome, and "Golgi apparatus" was also the most enriched GO-term in the protein cluster, nearly completely sequestered to LDs after 12 weeks of HFD (Figure 4A). Indeed, all proteins correlating with the profile of the Golgi markers, present under LFD and

**Figure 5. Establishment of Organelle Contacts under HFD**

(A) Comparison of the median mitochondrial marker profile at different time points of HFD reveals an additional LD peak in FR1 after 12 weeks of HFD.

(B) Quantification of LD-mitochondrial contact sites in electron microscopy images indicates a significant increase in the number of mitochondria interacting with LDs under HFD (Student's t test, p value < 0.01).

(C) Profile of the contact site proteins VPS13A overlaid with mitochondrial and LD marker profiles reveals a relocalization from mitochondrial to dual LD-mitochondrial localization under HFD.

(D) Profile of VPS13D overlaid with mitochondrial and LD marker profiles indicates loclaization under HFD.

(E) Immunofluorescence of VPS13A (green) and the LD marker PLIN2 (red) in liver slices of LFD and 12-week HFD mice shows relocalization of the contact site proteins to LDs and increased co-localization with PLIN2 under HFD.

(F) Immunofluorescence of VPS13D (green) and the LD marker PLIN2 (red) in LFD and HFD12 liver slices also indicates increased LD localization.

(G and H) Unsupervised hierarchical clustering of the *Z* scored intensities of phosphorylation sites on VPS13A (G) and VPS13D (H). Phosphopeptide levels were normalized to protein levels. Significantly changed sites are marked with black boxes (Student's t test, FDR 0.2).

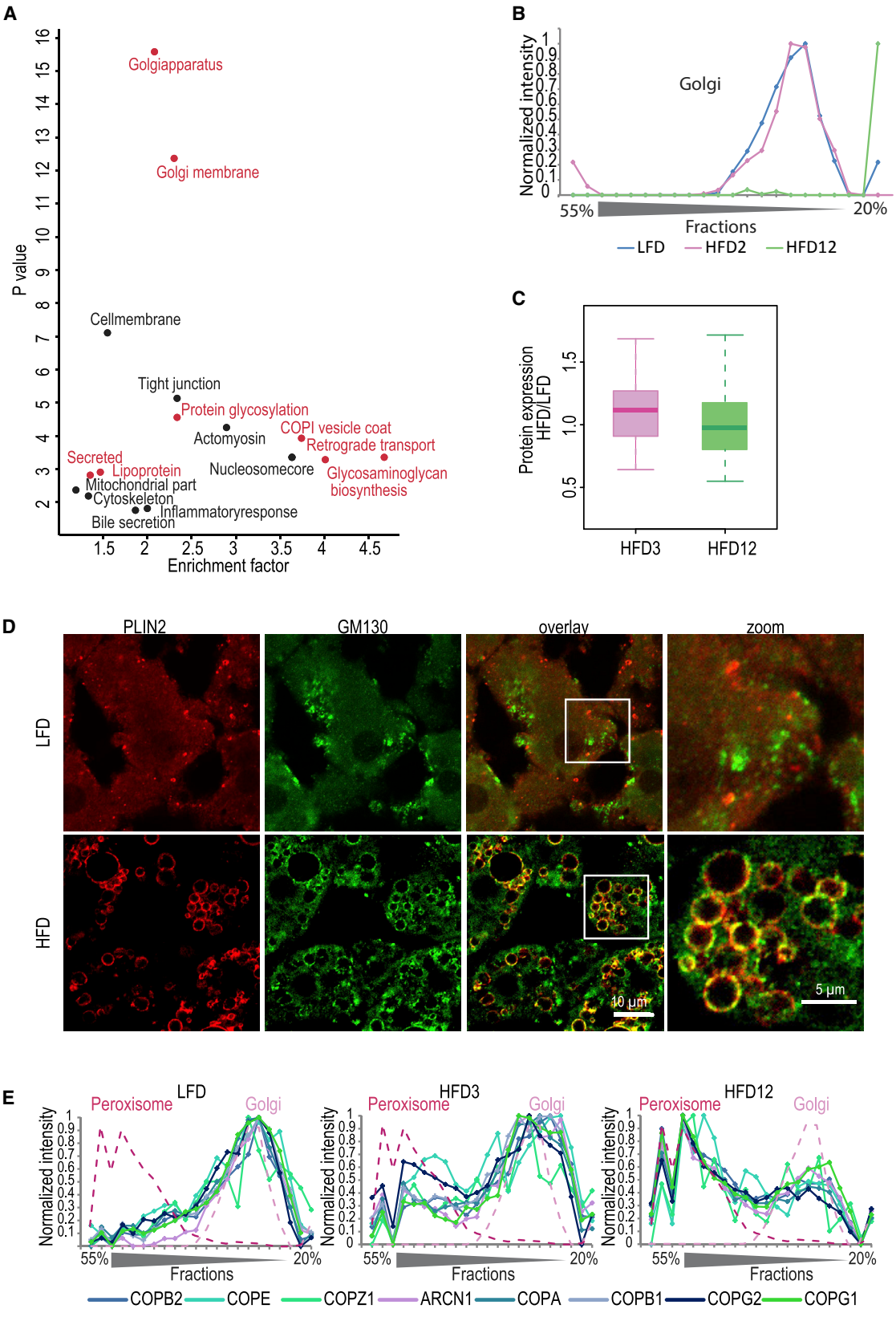


*(legend on next page)*

3 weeks of HFD, lost their characteristic organellar peak and moved into the LD fraction (Figure 6B). This drastic shift is due to relocalization because expression levels of marker Golgi apparatus proteins remained constant during our time course (Figure 6C).

We attempted to remove Golgi apparatus proteins from the LD fraction by an additional high-speed ultracentrifugation step in a non-sucrose-containing buffer. With this centrifugation step, all other contaminating membranous components or protein complexes, such as proteasomal subunits, were pelleted, whereas LD and Golgi marker proteins were even more enriched in the top LD fraction (Figure S7A). This might indicate a direct association between LDs and the Golgi apparatus proteins.

We were able to reconstitute the targeting of the Golgi apparatus to LDs *in vitro* by incubating LDs from mice with cell lysate from untreated rat hepatoma McA-RH7777 (McArdle) cells expressing a red fluorescence protein (RFP)-labeled Golgi marker. After the incubation period, LDs were floated a second time, and the amount of LD-targeted RFP was quantified by MS. This was much higher in the HFD than in the LFD condition, while protein levels in McArdle lysate and LD fractions were equal in all conditions (Figure S7B). The RFP marker was not detectable in the soluble fraction underneath the buoyant lipid layer. This finding supports direct association of the Golgi apparatus or Golgi proteins with LDs.

We further confirmed the relocalization of Golgi markers around LDs during steatosis by immunofluorescence microscopy analyses of GM130 and GOLGA5 in liver slices (Figures 6D and S7C). Specificity of the antibodies for the Golgi apparatus was confirmed in cell lines using brefeldin treatment, which disrupts Golgi morphology. In the LFD control, we observed GM130, a *cis*-Golgi marker, only around very few, mainly large LDs. Otherwise, it was confined to small vesicular structures most likely representing *cis*-Golgi structures in the liver tissue. After 12 weeks of HFD, when their proteomic localization profiles completely overlapped, GM130 extensively co-localized with the LD marker PLIN2 in a punctuate pattern (Figure 5D). We obtained similar results for GOLGA5. This general marker for the Golgi compartment also co-localized with LDs in the HFD condition. However, in addition, to punctuate clusters on the LDs, we also observed larger GOLGA5-positive Golgi cisternae accumulating around LDs. A 3D reconstruction based on those confocal images indicates a wrapping of Golgi compartments around LDs (Figures S7C–S7E, Video S1).

To more directly image the interaction between LDs and the Golgi apparatus, we next used stimulated emission depletion (STED) microscopy and DNA-PAINT, a recently developed optical super-resolution method that allows probing in the nanometer range (Schnitzbauer et al., 2017). In the liver of 12-week HFD mice, these technologies confirmed a direct co-localization of GOLGA5 with PLIN2 on the LD monolayer in a punctuate pattern and additional attachment of vesicles and larger cisternae positive for GOLGA5 directly to the LDs (Figures S7F and S7G). In addition, we imaged the LD-Golgi apparatus association in oleate-loaded McArdle cells by DNA-PAINT. In contrast to most other tested hepatic cell lines, Golgi relocalization can be induced in this system by loading with oleate for 72 hr. Again, results were consistent with a direct association between Golgi compartments and LDs (Figure S7H).

COPI and COPII complexes mediate retro- and anterograde trafficking between the Golgi apparatus and ER, respectively. Interestingly, the COPI complex was one of the most significantly enriched categories of relocalized proteins (Figure 4A). Accordingly, the fractionation profiles of all COPI subunits shifted significantly, whereas the COPII subunit profiles remained stable (Figure 6E).

To investigate if loss of the characteristic Golgi morphology and COPI localization affects protein secretion, we set up an MS-based proteomic secretion screen (Meissner et al., 2013). Whereas secretion of primary hepatocytes isolated after 3 weeks of HFD (Figures 7A and 7B) was not generally impaired, primary hepatocytes isolated after 12 weeks of HFD showed a significant decrease in the amount of secreted proteins in the supernatant, relative to primary hepatocytes from LFD mice (Figure 7C). On average, proteins annotated as secreted decreased 2-fold, with several proteins up to 4-fold reduced (Figure 7D). Interestingly, this reduction of protein secretion was even more pronounced when primary hepatocytes from HFD mice were cultured in the presence of FAs prior to the secretion assay (Figures 7E and 7F). In contrast, after starvation for several hours in serum-free medium, cells completely recovered from the secretion defect, indicating that loss of Golgi function is reversible and that the FAs themselves are causing the observed phenotype (Figures 7G and 7H; Table S8).

## DISCUSSION

This study offers a systems view of *in vivo* subcellular reorganization during the development of hepatic steatosis. High sensitivity, state-of-the-art, MS-based proteomic and phosphoproteomic workflows assigned cellular localization for almost 6,000 proteins and more than 16,000 phosphopeptides and quantified their changes in liver cells in their native environment accompanying progressive lipid accumulation in steatosis. Our data mainly reflect the response of hepatocytes to HFD, as we previously showed that the proteome of liver lysate highly

**Figure 6. Changes in Golgi Structure and Function under HFD**

(A) Enrichment and significance of selected representative GO-annotations, KEGG pathways, and keywords among the relocalized proteins after 12 weeks of HFD. Terms associated with the secretory pathway are indicated in red.

(B) Loss of the characteristic Golgi peak under HFD. Median Golgi marker profiles at different time points of HFD shows the loss of the characteristic peak at the late time point of HFD and a shift of the Golgi marker profile to the LD fraction (FR1).

(C) Boxplot showing fold changes of protein levels of all Golgi marker proteins at both time points of HFD indicates no significant effect on global Golgi protein levels under HFD.

(D) Immunofluorescence of the *cis*-Golgi apparatus marker GM130 (red) and the LD marker PLIN2 (green) in liver slices of LFD and 12-week HFD mice shows relocalization of GM130 to LDs and increased co-localization with PLIN2 under HFD.

(E) Protein profiles of all quantified COPI subunits in the liver of LFD and 3-week- and 12-week-HFD mice show increasing overlap with peroxisomal marker and loss of the Golgi peak profile over time.

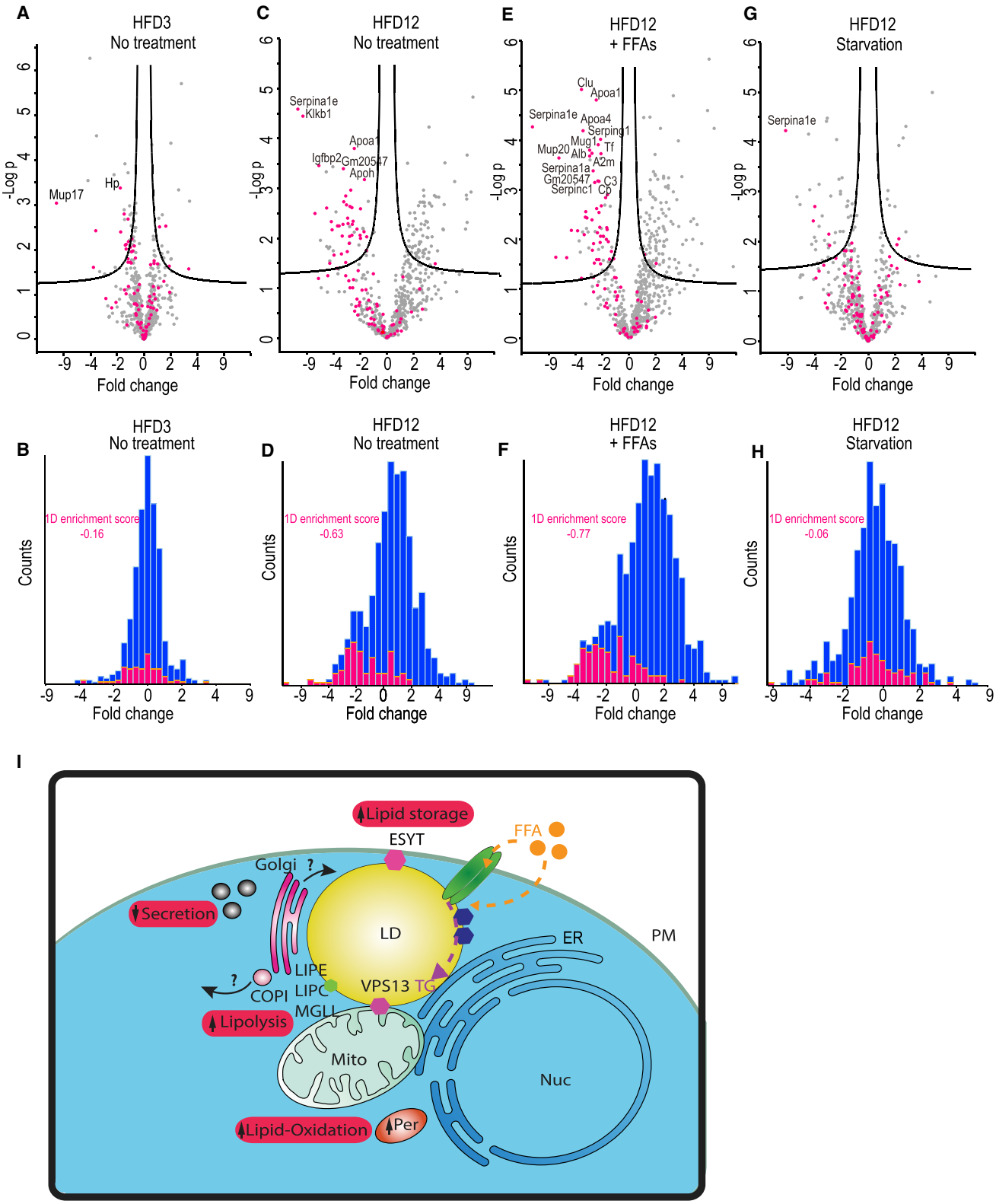


**Figure 7. Reduction of Protein Secretion under HFD and Model for Subcellular Reorganization Induced by Lipid Overload**

(A) Volcano plot representing fold changes of all proteins quantified in secretion assay performed in primary hepatocytes from HFD3 mice. Gene names of most significantly changed secreted proteins among three biological replicates are indicated (FDR 0.05). Proteins GO-annotated as secreted are pink.

*(legend continued on next page)*

correlates with the proteome of purified hepatocytes (Pearson correlation > 0.97) (Azimifar et al., 2014). Our systematic and unbiased approach reveals a progressive reorganization of subcellular structures from early insulin resistance to hepatosteatosis. Integration of different layers of proteomic and phosphoproteomic analysis revealed so far completely unknown protein relocalization events and cellular processes accompanying lipid accumulation. We also discovered new proteins that could play a role in the development of non-alcoholic fatty liver disease (NAFLD) and potentially serve as biomarkers or drug targets in the future. Along with the raw data, profiles for all quantified proteins and phosphosites under all conditions are freely accessible. All profiles can be visualized and overlaid with organelle marker profiles in our profile database (http://nafld-organellemap.org).

At early time points, where insulin resistance had already manifested but hepatic lipid levels were only slightly increased, we found a relocalization of important modulators of cellular signaling, vesicular trafficking, lipid metabolism, and a transcription factor. During prolonged HFD changes in global protein levels revealed a strong metabolic reprogramming toward lipid usage and accumulation in response to excess dietary lipid exposure (Figure 7I). These proteomic changes reflect cellular adaptions to the increased lipid levels. At the same time, we observed a drastic global cellular reorganization affecting the organellar association of more than 20% of the proteome. About a quarter of the significantly changed phosphorylation events during progression are on these proteins. Those phosphorylation changes may either cause the relocalization or be a consequence of it.

The formation of contact sites under a prolonged HFD was particularly intriguing because they could orchestrate metabolism in response to the lipid challenge. For instance, contacts between LDs and plasma membrane and between LDs and mitochondria may facilitate efficient substrate flux between these three cellular compartments. Such an arrangement would counteract lipotoxicity by direct storage of FAs in the form of TGs in LDs and support the channeling of FAs remobilized from LDs into mitochondria for β-oxidation. LD accumulation close to mitochondria has recently been suggested to protect mitochondrial function by sequestering toxic lipid species and shielding mitochondria (Nguyen et al., 2017). Although interactions of LDs with various other organelles have been reported (Schuldiner and Bohnert, 2017), the architecture of those associations and tethering factors have not been identified so far. The contact site proteins that we found to relocalize to LDs might therefore be interesting candidates to mediate the tethering of membranes implied in this model. Elucidating the roles of the contact sites and their tethers have in the development of hepatic steatosis and how the detected phosphorylation changes under HFD are related to the protein localization and functions will be exciting future research directions.

Although FAs' sequestration in LDs protects the cell from lipotoxicity (Neuschwander-Tetri, 2010), we unexpectedly observed that very extensive LD accumulation has a profound impact on cellular organization. Under steatotic conditions (4-fold increase in lipid content), a substantial fraction of the proteome (more than 6%), is targeted to the LD surface. We identified many new LD proteins that might have novel functions on the LDs and extend the known cellular role of LDs. Interestingly, some proteins identified before on LDs, such as DGAT2, did not show LD localization in our experiments. DGAT2 was found to be required for localized TG synthesis on LDs and LD growth (Wilfling et al., 2013). However, the LD proteome is highly dynamic, and some LD proteins might localize to LDs only under specific conditions, such as starvation or other time points of HFD. In addition, some proteins might be tissue- or cell type-specific. Differences of LD formation and growth in tissues and cell types are still poorly understood.

Our LD proteome also comprises proteins from diverse compartments and functions other than lipid metabolism. These include Rab proteins, small G-proteins, protein kinases, SNAREs, and other proteins involved in vesicular transport. This observation raises the question of what causes the retargeting of proteins normally binding to other cellular organelles to the LDs under HFD. Although the binding motifs and mechanisms of protein targeting to LDs are still poorly understood, it is known that different hydrophobic domains such as hairpin structures, amphipathic alpha helices, or lipid modifications can bind to the LD surface monolayer (Kory et al., 2016). Furthermore, the binding of those proteins seems to be partially determined by competition for limited sites on the LD surface

(B) Histogram of fold changes of all proteins quantified in secretion assay performed in primary hepatocytes from HFD3 mice. Proteins GO-annotated as secreted are shown in pink. 1D-annotation enrichment score for secreted proteins is indicated.
(C) Volcano plot of secretion assay performed in primary hepatocytes from HFD12 mice indicates a general reduction of protein secretion.
(D) Histogram of fold changes of all proteins quantified in secretion assay performed in primary hepatocytes from HFD12 mice.
(E) Volcano plot of secretion assay performed in primary hepatocytes from HFD12 mice indicates a general reduction of protein secretion when hepatocytes were incubated overnight with FA-BSA before a secretion assay was performed.
(F) Histogram of protein fold changes in secretion assay performed in primary hepatocytes from HFD12 mice when hepatocytes were incubated overnight with FA-BSA before a secretion assay was performed.
(G) Volcano plot of secretion assay performed in primary hepatocytes from HFD12 mice that were starved in serum free media for 4hrs before the secretome analysis was performed indicates recovery of the secretion defect.
(H) Histogram of protein fold changes in secretion assay performed in primary hepatocytes from HFD12 mice that were starved in serum free media for 4hrs before the secretome analysis.
(I) Under HFD, cells are challenged with large amounts of FAs. To prevent lipotoxicity, FAs are sequestered in the form of TGs into LDs. Close contacts between plasma membrane and LDs might facilitate direct channeling of FAs into LDs. Contacts between mitochondria and LDs would enable efficient substrate flux of FA released from LDs by lipolysis. Expansion of LD surfaces might provide binding sites for proteins with hydrophobic patches, sequestering proteins from other cellular organelles, interfering with cellular and organ functions. A tethering of the Golgi apparatus, mis-localization of the Golgi-ER trafficking complex COPI might contribute to a reduction of the secretory capacity of the hepatocytes. This concomitant overflow of lipids and incapability to secrete might lead to a vicious cycle contributing to the manifestations of severe steatosis.

(Kory et al., 2015). Under steatosis, the expanded LD surface provides new protein binding sites and may sequester proteins with lower monolayer binding affinities from other cellular compartments. The expanding LDs may thus act as protein sink, depleting proteins from different sources and thereby interfering with multiple cellular processes. The dramatic extent of this sequestering and our findings suggest a new view on LDs and their role in pathologies.

The most striking result from our proteomic profiling experiment is the relocalization of the Golgi apparatus and its sequestering to LDs. We confirmed this proteomic discovery with complementary biochemical and microscopy-based approaches. Confocal fluorescence microscopy and different super-resolution microscopy-based approaches indicate that small vesicles and larger fragments of the Golgi apparatus directly attach to LDs. Most Golgi proteins do not have structural features enabling direct monolayer binding, suggesting that Golgi membranes or fragments are recruited through specific proteins with a tethering role. It will be interesting to identify those tethering proteins. Potential candidates might be Golgi organizers that contain amphipathic lipid packing sensors (ALPSs), motifs that sense membrane curvature and membrane packing defects and have been found to bind directly to the LD surface (Prévost et al., 2018). Artificial targeting of GMAP210 leads to Golgi accumulation around mitochondria (Wong and Munro, 2014), and a similar process could occur when ALPSs' domain proteins are sequestered to LDs under conditions of major LD surface expansion.

It would be interesting to investigate a potential causal connection of Golgi to COPI relocalization, since impairment of retrograde transport also has a strong impact on Golgi apparatus structure and function (Saitoh et al., 2009). Finally, changes of Golgi structure under HFD may also be controlled by signaling pathways and phosphorylation events as is the case for Golgi disassembly and assembly during the cell cycle (Kano et al., 2000). Consistent with this, we observe an enrichment of Golgi proteins and many important Golgi organizers among the proteins with phosphorylation changes.

Our data establish that HFD has a strong impact on Golgi structure, localization, and its secretory function. Interestingly, the secretion defect is dependent on lipid overload and can rapidly be reversed by starvation in our cellular model. In addition to the observed changes in Golgi apparatus localization, increased cellular FAs could impact ER lipid composition, ER stress, and ER secretory function and thereby influence protein secretion at different cellular stages.

In primary hepatocytes from HFD mice, most secreted proteins are reduced in the cellular supernatant, including ApoB, indicating that Golgi apparatus relocalization might, in addition to its general influence on protein secretion, also influence lipoprotein secretion. Indeed, previous *in vivo* assays had found reduced VLDL secretion upon HFD (Cahova et al., 2012; Gibbons and Pullinger, 1987). These reports support our findings of HFD-induced reduction in hepatic secretion *in vivo*, and our Golgi sequestration model might be a factor contributing to these observations.

The attendant reorganization of the secretory apparatus and the changes in cellular secretion may represent a mechanism contributing to the development of NAFLD. In particular, the disruption of the secretory function under HFD could have severe physiological consequences, leading to a cycle of reduced lipoprotein secretion, which in turn enhances hepatic LD formation and steatosis. Indeed, impaired secretion of VLDL could further increase cytoplasmic LD accumulation and Golgi apparatus reorganization, resulting in a deleterious positive feedback loop that promotes fatty liver. Moving on from mouse models, it will be crucial in the future to investigate whether Golgi relocalization and the reduced protein secretion also occur in patients with NAFLD and how these contribute to the progression of NASH. Mechanisms to restore Golgi structure and secretion may prevent or delay the progression of hepatic steatosis.

In summary, our integrated proteomic analyses of the mouse liver under normal and HFD-induced steatosis provide a rich dataset that allows for unbiased studies of cellular and organellar changes. This enables the discovery of unexpected cellular processes, most prominently the sequestration of the Golgi apparatus to LDs. Our dataset provides the basis for the identification of so far unknown factors involved in the development of hepatic steatosis and will enable the discovery of new drug targets.

## STAR★METHODS

Detailed methods are provided in the online version of this paper and include the following:

- KEY RESOURCES TABLE
- CONTACT FOR REAGENT AND RESOURCE SHARING
- EXPERIMENTAL MODEL AND METHOD DETAILS
  - Experimental Model
- METHOD DETAILS
  - Hepatocyte Isolation and Culturing
  - Histology
  - Site-Directed Mutagenesis and Expression of Constructs
  - Western Blot
  - Confocal Microscopy
  - DNA-PAINT
  - STED Microscopy
  - Electron Tomography and Quantification of LD-Mitochondria Contact Sites
  - Protein- and phosphopeptide correlation profiling
  - *In Vitro* Assay for Golgi Apparatus Targeting
  - Sample preparation for proteomic analysis
  - EasyPhos
  - MS Analysis
  - PRM Analyses
- QUANTIFICATION AND STATISTICAL ANALYSIS
  - Data Analysis
  - Proteome Analysis
  - Phosphoproteome Analysis
  - Secretome Analysis
  - Generation of Protein and Phosphopeptide Profiles
  - Organelle Assignments
  - Filtering of LD Proteins
  - Analysis of Changes of Organelle Proteomes
- DATA AND SOFTWARE AVAILABILITY
  - Data Resources

## SUPPLEMENTAL INFORMATION

Supplemental Information includes seven figures, eight tables, and one video and can be found with this article online at https://doi.org/10.1016/j.devcel.2018.09.017.

## ACKNOWLEDGMENTS

We thank Jeffrey Liu for critical reading of the manuscript. We thank Dirk Wischnewski, Sebastian Krämer, Steven Dewitz, and Julia Wolf for technical assistance; and Morvan Graham and Xinran Liu (Yale School of Medicine) for performing EM. These studies were supported by the Center for Integrated Protein Science Munich (CIPSM) and the Virtual Liver Network. B.N. was supported by the DFG Grant ZE 1037/1-1 awarded to A.Z. F.Q. was supported by DFG Emmy Noether UH 275/1-1 (to N.H.U.). T.C.W. was supported by NIGMS (R01GM097194).

## AUTHOR CONTRIBUTIONS

M.M. and N.K. conceived the project. M.M. supervised the project. N.K., A.Z., and N.H.U. designed all experiments. N.K. and M.S. performed organelle fractionations, proteomic and phosphoproteomic analysis, immunostainings, and secretion analysis. B.N., S.S., and F.Q. dissected mice and isolated hepatocytes. N.K., F.Schueder, and R.K. performed microscopy. N.K. and G.H.H.B. analyzed the data. J.C. developed the software for data analysis. F.S. created the profile database. N.K., T.C.W., M.M., A.Z., and G.H.H.B. wrote the manuscript.

## DECLARATION OF INTERESTS

The authors declare no competing interests.

Received: March 16, 2018
Revised: June 29, 2018
Accepted: September 18, 2018
Published: October 22, 2018

## REFERENCES

Andersen, J.S., Wilkinson, C.J., Mayor, T., Mortensen, P., Nigg, E.A., and Mann, M. (2003). Proteomic characterization of the human centrosome by protein correlation profiling. Nature *426*, 570–574.

Azimifar, S.B., Nagaraj, N., Cox, J., and Mann, M. (2014). Cell-type-resolved quantitative proteomics of murine liver. Cell Metab. *20*, 1076–1087.

Bauer, N.C., Doetsch, P.W., and Corbett, A.H. (2015). Mechanisms regulating protein localization. Traffic *16*, 1039–1061.

Bersuker, K., Peterson, C.W.H., To, M., Sahl, S.J., Savikhin, V., Grossman, E.A., Nomura, D.K., and Olzmann, J.A. (2018). A proximity labeling strategy provides insights into the composition and dynamics of lipid droplet proteomes. Dev. Cell *44*, 97–112.e7.

Biddinger, S.B., Hernandez-Ono, A., Rask-Madsen, C., Haas, J.T., Alemán, J.O., Suzuki, R., Scapa, E.F., Agarwal, C., Carey, M.C., Stephanopoulos, G., et al. (2008). Hepatic insulin resistance is sufficient to produce dyslipidemia and susceptibility to atherosclerosis. Cell Metab. *7*, 125–134.

Brasaemle, D.L., and Wolins, N.E. (2016). Isolation of lipid droplets from cells by density gradient centrifugation. Curr. Protoc. Cell Biol. *72*, 3.15.1–3.15.13.

Cahova, M., Dankova, H., Palenickova, E., Papackova, Z., and Kazdova, L. (2012). The opposite effects of high-sucrose and high-fat diet on fatty acid oxidation and very low density lipoprotein secretion in rat model of metabolic syndrome. J. Nutr. Metab. *2012*, 757205.

Christoforou, A., Mulvey, C.M., Breckels, L.M., Geladaki, A., Hurrell, T., Hayward, P.C., Naake, T., Gatto, L., Viner, R., Martinez Arias, A.M., et al. (2016). A draft map of the mouse pluripotent stem cell spatial proteome. Nat. Commun. *7*, 8992.

Cohen, J.C., Horton, J.D., and Hobbs, H.H. (2011). Human fatty liver disease: old questions and new insights. Science *332*, 1519–1523.

Cox, J., and Mann, M. (2008). MaxQuant enables high peptide identification rates, individualized p.p.b.-range mass accuracies and proteome-wide protein quantification. Nat. Biotechnol. *26*, 1367–1372.

Deeb, S.J., Tyanova, S., Hummel, M., Schmidt-Supprian, M., Cox, J., and Mann, M. (2015). Machine learning-based classification of diffuse large B-cell lymphoma patients by their protein expression profiles. Mol. Cell Proteomics *14*, 2947–2960.

Foster, L.J., de Hoog, C.L., Zhang, Y.L., Zhang, Y., Xie, X.H., Mootha, V.K., and Mann, M. (2006). A mammalian organelle map by protein correlation profiling. Cell *125*, 187–199.

Gao, Q., and Goodman, J.M. (2015). The lipid droplet-a well-connected organelle. Front. Cell Dev. Biol. *3*, 49.

Gibbons, G.F., and Pullinger, C.R. (1987). Regulation of hepatic very-low-density lipoprotein secretion in rats fed on a diet high in unsaturated fat. Biochem. J. *243*, 487–492.

Gnad, F., Forner, F., Zielinska, D.F., Birney, E., Gunawardena, J., and Mann, M. (2010). Evolutionary constraints of phosphorylation in eukaryotes, prokaryotes, and mitochondria. Mol. Cell Proteomics *9*, 2642–2653.

Grimsrud, P.A., Carson, J.J., Hebert, A.S., Hubler, S.L., Niemi, N.M., Bailey, D.J., Jochem, A., Stapleton, D.S., Keller, M.P., Westphall, M.S., et al. (2012). A quantitative map of the liver mitochondrial phosphoproteome reveals posttranslational control of ketogenesis. Cell Metab. *16*, 672–683.

Guo, Y., Darshi, M., Ma, Y., Perkins, G.A., Shen, Z., Haushalter, K.J., Saito, R., Chen, A., Lee, Y.S., Patel, H.H., et al. (2013). Quantitative proteomic and functional analysis of liver mitochondria from high fat diet (HFD) diabetic mice. Mol. Cell Proteomics *12*, 3744–3758.

Humphrey, S.J., Azimifar, S.B., and Mann, M. (2015). High-throughput phosphoproteomics reveals in vivo insulin signaling dynamics. Nat. Biotechnol. *33*, 990–995.

Humphrey, S.J., Yang, G., Yang, P., Fazakerley, D.J., Stöckli, J., Yang, J.Y., and James, D.E. (2013). Dynamic adipocyte phosphoproteome reveals that Akt directly regulates mTORC2. Cell Metab. *17*, 1009–1020.

Itzhak, D.N., Tyanova, S., Cox, J., and Borner, G.H.H. (2016). Global, quantitative and dynamic mapping of protein subcellular localization. Elife *5*, e16950.

Jobert, L., Argentini, M., and Tora, L. (2009). PRMT1 mediated methylation of TAF15 is required for its positive gene regulatory function. Exp. Cell Res. *315*, 1273–1286.

Kano, F., Takenaka, K., Yamamoto, A., Nagayama, K., Nishida, E., and Murata, M. (2000). MEK and Cdc2 kinase are sequentially required for Golgi disassembly in MDCK cells by the mitotic Xenopus extracts. J. Cell Biol. *149*, 357–368.

Kory, N., Farese, R.V., Jr., and Walther, T.C. (2016). Targeting fat: mechanisms of protein localization to lipid droplets. Trends Cell Biol. *26*, 535–546.

Kory, N., Thiam, A.R., Farese, R.V., Jr., and Walther, T.C. (2015). Protein crowding is a determinant of lipid droplet protein composition. Dev. Cell *34*, 351–363.

Krahmer, N., Farese, R.V., Jr., and Walther, T.C. (2013a). Balancing the fat: lipid droplets and human disease. EMBO Mol. Med. *5*, 973–983.

Krahmer, N., Hilger, M., Kory, N., Wilfling, F., Stoehr, G., Mann, M., Farese, R.V., Jr., and Walther, T.C. (2013b). Protein correlation profiles identify lipid droplet proteins with high confidence. Mol. Cell Proteomics *12*, 1115–1126.

Kulak, N.A., Pichler, G., Paron, I., Nagaraj, N., and Mann, M. (2014). Minimal, encapsulated proteomic-sample processing applied to copy-number estimation in eukaryotic cells. Nat. Methods *11*, 319–324.

Lang, A.B., John Peter, A.T., Walter, P., and Kornmann, B. (2015). ER-mitochondrial junctions can be bypassed by dominant mutations in the endosomal protein Vps13. J. Cell Biol. *210*, 883–890.

Lees, J.A., Messa, M., Sun, E.W., Wheeler, H., Torta, F., Wenk, M.R., De Camilli, P., and Reinisch, K.M. (2017). Lipid transport by TMEM24 at ER-plasma membrane contacts regulates pulsatile insulin secretion. Science *355*, 709.

Meissner, F., Scheltema, R.A., Mollenkopf, H.J., and Mann, M. (2013). Direct proteomic quantification of the secretome of activated immune cells. Science *340*, 475–478.

Neuschwander-Tetri, B.A. (2010). Nontriglyceride hepatic lipotoxicity: the new paradigm for the pathogenesis of NASH. Curr. Gastroenterol. Rep. *12*, 49–56.

Newton, P.M., and Messing, R.O. (2010). The substrates and binding partners of protein kinase cepsilon. Biochem. J. *427*, 189–196.

Nguyen, T.B., Louie, S.M., Daniele, J.R., Tran, Q., Dillin, A., Zoncu, R., Nomura, D.K., and Olzmann, J.A. (2017). DGAT1-dependent lipid droplet biogenesis protects mitochondrial function during starvation-induced autophagy. Dev. Cell *42*, 9–21.e25.

Papáčková, Z., Daňková, H., Páleníčková, E., Kazdová, L., and Cahová, M. (2012). Effect of short- and long-term high-fat feeding on autophagy flux and lysosomal activity in rat liver. Physiol. Res. *61*, S67–SS76.

Petersen, M.C., Madiraju, A.K., Marcel, M., Gassaway, B.M., Nasiri, A.R., Butrico, G., Marcucci, M.J., Zhang, D.Y., Zhang, X.M., Philbrick, W., et al. (2016). Insulin receptor Thr1160 phosphorylation mediates lipid-induced hepatic insulin resistance. Diabetes *65*, A13.

Peterson, A.C., Russell, J.D., Bailey, D.J., Westphall, M.S., and Coon, J.J. (2012). Parallel reaction monitoring for high resolution and high mass accuracy quantitative, targeted proteomics. Mol. Cell Proteomics *11*, 1475–1488.

Prévost, C., Sharp, M.E., Kory, N., Lin, Q.Q., Voth, G.A., Farese, R.V., and Walther, T.C. (2018). Mechanism and determinants of amphipathic helix-containing protein targeting to lipid droplets. Dev. Cell *44*, 73–86.e4.

Saheki, Y., Bian, X., Schauder, C.M., Sawaki, Y., Surma, M.A., Klose, C., Pincet, F., Reinisch, K.M., and De Camilli, P. (2016). Control of plasma membrane lipid homeostasis by the extended synaptotagmins. Nat. Cell Biol. *18*, 504–515.

Saitoh, A., Shin, H.W., Yamada, A., Waguri, S., and Nakayama, K. (2009). Three homologous ArfGAPs participate in coat protein I-mediated transport. J. Biol. Chem. *284*, 13948–13957.

Schindelin, J., Arganda-Carreras, I., Frise, E., Kaynig, V., Longair, M., Pietzsch, T., Preibisch, S., Rueden, C., Saalfeld, S., Schmid, B., et al. (2012). Fiji: an open-source platform for biological-image analysis. Nat. Methods *9*, 676–682.

Schnitzbauer, J., Strauss, M.T., Schlichthaerle, T., Schueder, F., and Jungmann, R. (2017). Super-resolution microscopy with DNA-PAINT. Nat. Protoc. *12*, 1198–1228.

Schueder, F., Lara-Gutiérrez, J., Beliveau, B.J., Saka, S.K., Sasaki, H.M., Woehrstein, J.B., Strauss, M.T., Grabmayr, H., Yin, P., and Jungmann, R. (2017). Multiplexed 3D super-resolution imaging of whole cells using spinning disk confocal microscopy and DNA-PAINT. Nat. Commun. *8*, 2090.

Schuldiner, M., and Bohnert, M. (2017). A different kind of love - lipid droplet contact sites. Biochim. Biophys. Acta *1862*, 1188–1196.

Thul, P.J., Åkesson, L., Wiking, M., Mahdessian, D., Geladaki, A., Ait Blal, H.A., Alm, T., Asplund, A., Björk, L., Breckels, L.M., et al. (2017). A subcellular map of the human proteome. Science *356*, 820.

Tyanova, S., Temu, T., and Cox, J. (2016). The MaxQuant computational platform for mass spectrometry-based shotgun proteomics. Nat. Protoc. *11*, 2301–2319.

Wilfling, F., Wang, H., Haas, J.T., Krahmer, N., Gould, T.J., Uchida, A., Cheng, J.X., Graham, M., Christiano, R., Fröhlich, F., et al. (2013). Triacylglycerol synthesis enzymes mediate lipid droplet growth by relocalizing from the ER to lipid droplets. Dev. Cell *24*, 384–399.

Wong, M., and Munro, S. (2014). Membrane trafficking. The specificity of vesicle traffic to the Golgi is encoded in the golgin coiled-coil proteins. Science *346*, 1256898.

Vizcaino, J.A., Deutsch, E.W., Wang, R., Csordas, A., Reisinger, F., Rios, D., Dianes, J.A., Sun, Z., Farrah, T., Bandeira, N., et al. (2014). ProteomeXchange provides globally coordinated proteomics data submission and dissemination. Nat. Biotechnol. *32*, 223–226.

Xiu, L.C., Lin, M.H., Liu, W.W., Kong, D.L., Liu, Z.H., Zhang, Y., Ouyang, P., Liang, Y., Zhong, S.Q., Chen, C., et al. (2015). Association of DRD3, COMT, and SLC6A4 gene polymorphisms with type 2 diabetes in Southern Chinese: a hospital-based case-control study. Diabetes Technol. Ther. *17*, 580–586.

Yang, D.Q., and Kastan, M.B. (2000). Participation of ATM in insulin signalling through phosphorylation of eIf-4E-binding protein 1. Nat. Cell Biol. *2*, 893–898.

Zehmer, J.K., Bartz, R., Bisel, B., Liu, P.S., Seemann, J., and Anderson, R.G.W. (2009). Targeting sequences of UBXD8 and AAM-B reveal that the ER has a direct role in the emergence and regression of lipid droplets. J. Cell Sci. *122*, 3694–3702.

Zeigerer, A., Gilleron, J., Bogorad, R.L., Marsico, G., Nonaka, H., Seifert, S., Epstein-Barash, H., Kuchimanchi, S., Peng, C.G., Ruda, V.M., et al. (2012). Rab5 is necessary for the biogenesis of the endolysosomal system in vivo. Nature *485*, 465–470.

## STAR★METHODS

### KEY RESOURCES TABLE

| REAGENT or RESOURCE | SOURCE | IDENTIFIER |
|---|---|---|
| Antibodies | | |
| Alexa Fluor 488 Goat anti-Rabbit, 1:1000 | Thermo Fisher Scientific | A32731; RRID: AB_2633280 |
| Alexa Fluor 555 Goat anti-Guinea Pig, 1:1000 | Thermo Fisher Scientific | A-11073; RRID: AB_142018 |
| FluoTag®-X2 anti-Guinea Pig, IgG Abberior® Star 580 | Nano-Tag | N0602-Ab580-S |
| FluoTag®-X2 anti-Rabbit, IgG Abberior® Star Red | Nano-Tag | N1002-AbRED-S |
| Alexa Fluor 647 Goat anti-Rabbit, 1:500 | Thermo Fisher Scientific | A-21245; RRID: AB_2535813 |
| Rabbit monoclonal anti-GM130, 1:200 | Abcam | ab52649; RRID: AB_880266 |
| Rabbit polyclonal anti-GOLGA5, 1:200 | Atlas Antibodies | HPA000992; RRID: AB_1079009 |
| Guinea pig polyclonal anti-PLIN2, 1:200 | Progen | GP40 |
| Rabbit polyclonal anti-TOM20, 1:500 | Santa Cruz | sc-11415; RRID: AB_2207533 |
| Rabbit polyclonal anti-ESYT2, 1:100 | Atlas Antibodies | HPA002132; RRID: AB_1078807 |
| Rabbit polyclonal anti-VPS13A, 1:100 | Atlas Antibodies | HPA021652 |
| Rabbit polyclonal anti-Mettl7A, 1:100 | Invitrogen | PA5-20635; RRID: AB_1858759 |
| Rabbit polyclonal anti-PRKC epsilon 1:500 | Cell signaling | 2683S; RRID: AB_2171906 |
| Rabbit polyclonal anti-βACTIN 1:1000 | Cell Signaling | 4967; RRID: AB_330288 |
| Rabbit polyclonal anti-VPS13D, 1:100 | Atlas Antibodies | HPA051621; RRID: AB_2681555 |
| Chemicals, Peptides, and Recombinant Proteins | | |
| Protease inhibitor | Roche Diagnostics | 04693132001 |
| Phosphatase inhibitor | Roche Diagnostics | 04693159001 |
| Lysyl Endopeptidase LysC | Wako Chemicals | 129-02541 |
| Trypsin | Sigma-Aldrich | T6567 |
| Embed 812 | Electron Microscopy Sciences | 14120 |
| Sodium cacodylate buffer pH7.4 | Electron Microscopy Sciences | 11653 |
| 25% Glutaraldehyde | Electron Microscopy Sciences | 16200 |
| 16% Paraformaldehyde | Electron Microscopy Sciences | 15700 |
| DAPI | Thermo Fisher Scientifc | D3571 |
| Alexa Fluor 488 Phalloidin | Thermo Fisher Scientifc | A12379 |
| BODIPY 493/503 | Thermo Fisher Scientific | D3922 |
| Critical Commercial Assays | | |
| Triglyceride Colorimetric Assay | Cayman | 10010303 |
| Deposited Data | | |
| PRIDE | Dataset identifier: PXD007653<br>Password: DoYsjWv1 | http://www.proteomexchange.org/ |
| Mouse UniprotKB/Swiss-Prot database (Mouse UniProt 2014-07) | N/A | http://www.uniprot.org/proteomes |
| Experimental Models: Organisms/Strains | | |
| C57BL/6J mice | Javier Labs | N/A |
| LFD Surwit diet, 11% kcal fat | Research Diets | D12329 |
| HFD Surwit diet, 58% kcal fat | Research Diets | D12331 |
| Software and Algorithms | | |
| MaxQuant version 1.5.1.6 | Cox and Mann, 2008 | http://www.biochem.mpg.de5111795/maxquant |
| Perseus version 1.5.6.2 | Tyanova et al., 2016 | http://www.biochem.mpg.de/5111810/perseus |
| Fiji Life-Line version | NIH | N/A |

## CONTACT FOR REAGENT AND RESOURCE SHARING

Requests for further information and reagents may be directed to the Lead Contact, Matthias Mann (mmann@biochem.mpg.de).

## EXPERIMENTAL MODEL AND METHOD DETAILS

### Experimental Model

#### *Mouse Model*

At the age of 4 weeks male C57BL/6J were set on the following diets: control mice were kept on LFD for 12 weeks, HDF3 mice were kept on LFD for 9 weeks and then switched to HFD for 3 weeks, and HFD12 mice were kept on HFD for 12 weeks. For HFD we used Surwit diet, Research Diets, D12329, 58 kcal% fat w/sucrose and LFD control mice were fed with Surwit diet, Research Diets D12331, 11 kcal% fat w/sucrose. Mice were sacrificed at the age of 16 weeks in an ad libitum fed state in accordance with an approved protocol (Animal Protection Institute of Upper Bavaria 55.2-1-54-2532-164-2015). Glucose tolerance was monitored by OGTT 3 days before dissecting the mice for the liver isolation. Animals were fasted for 6hrs, fasted blood glucose levels were determined before a solution of glucose (2g/kg body weight) was administered by oral gavage. Subsequently, blood glucose was measured at the indicated time points. Liver TG levels were determined by a calorimetric assay (Cayman's Triglyceride Assay Kit); the assay is based on the enzymatic hydrolysis of the triglycerides by lipase to produce glycerol and free fatty acids. The glycerol released is subsequently measured by a coupled enzymatic reaction system with a colorimetric readout at 540nm.

## METHOD DETAILS

### Hepatocyte Isolation and Culturing

Primary hepatocytes were isolated from mice via collagenase perfusion as previously described (Zeigerer et al., 2012). Cells were cultured in collagen gel-coated 24-well plates at 200,000 cells/well in Williams E medium, substituted with 10% FBS, 100nM dexamethasone and penicillin/streptomycin, and maintained at 37°C in an atmosphere with 5% $CO_2$. After 2hrs of attachment, cultures were washed with phosphate buffered saline (PBS) and incubated, when indicated with FAs (palmitate 100 μM and oleate 400 μM complexed with Bovine serum albumin (BSA) 1:6 (Brasaemle and Wolins, 2016) or BSA alone in Williams E medium with 10% FBS and penicillin/streptomycin for an additional 16hrs. Thereafter, cells were fixed in 4% paraformaldehyde (PFA) in PBS at room temperature for 15min, washed twice with PBS, permeabilized for 5-10min with 0.1% Triton X-100 in PBS, and washed and blocked in PBS with 10% horse serum for 10min. Cells were incubated with primary antibodies at room temperature for 1hr, washed three times with PBS and incubated with secondary antibodies for 1hr at RT (for antibodies see Key Resources Table). Thereafter cells were washed and mounted onto glass slides using 0.1g/ml Mowiol.

For the secretome analysis the primary hepatocytes were washed once with Williams E medium without FBS and incubated in 200μl/well in medium without FBS and FAs for 4hrs. Thereafter, the medium from three wells was pooled and analyzed by MS. Cells were lysed to determine the total protein content per well. Cell number and viability of the cells isolated from mice kept on the different diets were very similar.

### Histology

Livers of HFD12 and LFD mice were fixed by cardiac perfusion with 4% PFA in PBS for 10min, incubated in 4% PFA in PBS at 4°C overnight and stored in PBS until further use. Before embedding in optimal cutting temperature compound (OCT), liver pieces were transferred to 30% sucrose in PBS for three days. Next, cryostat sections of 5 to 7μm thickness were cut and collected on superfrost plus treated slides. Cryosections were sequentially immunolabeled with primary and secondary antibodies (Key Resources Table), by incubation in PBS containing 3% (w/v) BSA. Sections were then mounted with Mowiol onto coverslips for imaging.

### Site-Directed Mutagenesis and Expression of Constructs

Mettl7A S216A was generated by site-directed mutagenesis using a site-directed mutagenesis kit (Q5® Site-Directed Mutagenesis kit, NEB) with the following primers: Fwd 5'AGAGCAGGCCgcaTTCTCGAAGCTAAAG3', Rev 5'ATGGTCTTCCAGCTCTCTC3' from the plasmid pCMV6-AC-Mettl7A-GFP (MG203043, Origene). McArdle cells were cultivated in DMEM (10%FBS, Penecillin and Streptomycin) and transfected with Viromer red (Lipocalyx) according to manufacturer's instructions. 48hrs after transfection oleate treatment was started for the indicated times and cells were imaged by confocal microscopy in PBS (1:1000 HCS LipidTOX red neutral lipid stain, Thermo Fisher) after fixation with 4% PFA for 10min.

### Western Blot

For SDS-PAGE, 100μg of proteins of total liver lysate were separated in a 10% gradient gel and transferred to a PVDF membrane. The membrane was blotted with the primary antibody. After incubation with HRP-conjugated secondary antibodies, the bound antibodies were visualized by using an enhanced chemiluminescence (ECL) detection system and scanned using an ImageQuant LAS 4000 instrument (GE Healthcare).

### Confocal Microscopy

Samples were analyzed using a Zeiss LSM780 Confocal Laser Scanning Microscope (Max-Planck Institute for Biochemistry, core facility) with a Zeiss Plan-Apochromat 100x/1,46 Oil DIC objective at a resolution of app. 100μm/pixel. Images were analyzed using Fiji software (Schindelin et al., 2012). Presented images are maximal projections of three merged middle confocal sections. The three-dimensional movie renderings were made using IMARIS 9.1.0 'normal shading' rendering mode.

### DNA-PAINT

Cells and Tissue were fixed with 4% PFA. Samples were then blocked and permeabilized with 3% BSA and 0.25% Triton-X-100 for 2hrs. The Golgi apparatus was labeled using a primary antibody against GOLGA5 and a DNA-conjugated secondary anti-rabbit antibody (P5 DNA-Sequence) (Schnitzbauer et al., 2017). LDs were labeled using a primary antibody against PLIN2 and a DNA-conjugated secondary anti-guinea pig antibody (X61 DNA-Sequence). For DNA-PAINT in McArdle cells Cy3b-labeled imager strands were used at a concentration of 1nM P5 Sequence and 4nM X61 Sequence. For the imaging in liver slices a Cy3b-labeld imager strand (P5) and an Atto655 imager-labeled strand (X61) at a concentration of 5nM were used. For the cell experiment the laser power was set to 17mW (PLIN2-Anti-Guinea Pig-X61) and 20mW (GOLGA5-Anti-Rabbit-P5) at the sample plane. For the tissue experiment the power of the 640nm Laser was set to 69mW (PLIN2-Anti-Guinea Pig-X61) and for the 561nm Laser to 24mW (GOLGA5-Anti-Rabbit-P5).

| Name | Docking site Sequence at antibody | Imager Sequence |
|---|---|---|
| P5 | 5'-TT-TCAATGTATG-3' | 5'-CATACATTGA-Cy3b-3' |
| X61 | 5'-TT-TCCTCAATTA-3' | 5'- AATTGAGGA-Cy3b-3' |
| X61 | 5'-TT-TCCTCAATTA-3' | 5'- AATTGAGGA-Atto655-3' |

Confocal Setup: DNA-PAINT imaging was performed using an Andor Dragonfly Spinning Disk Confocal system (Andor) based on an inverted Nikon Eclipse Ti2 microscope (Nikon Instruments) with the Perfect Focus System, using an oil immersion objective (Plan Apo 100×, NA 1.45, Oil) (Schueder et al., 2017). For excitation, a 561nm laser (2 W, MPB) and a 640nm laser (2W, MPB) was used. The laser beam was passed through a beam conditioning unit (Andor Borealis) for reshaping the beam from a Gaussian profile to a flat top profile. Next, the beam was coupled into the Andor Dragonfly spinning disk unit, passed through the multi-pinhole disk with a pinhole size of 40μm and from there coupled into the objective lens. Excitation and emission light was spectrally split using a beam splitter (CR-DFLY-DMQD-01). Fluorescence light was spectrally filtered with an emission filter (TR-DFLY-F600-050 and TR-DFLY-F700-075) and imaged on an sCMOS camera (Andor Zyla 4.2 PLUS) without further magnification, resulting in an effective pixel size of 130nm (sCMOS after 2×2 binning). The disk speed was set to 6000rpm and an excitation field stop of 13.3mm × 13.3mm was applied.

### STED Microscopy

STED imaging was done on a STEDYCON microscope (Abberior Instruments) equipped with a 100×/1.4 Oil objective (Leica). PLIN2 and GOLGA5 were labeled with a two color immuno-fluorescence antibody combination. PLIN2 with either anti-rabbit Abberior® Star Red or anti-rabbit Alexa Fluor 647 and GOLGA5 with anti-guinea pig Abberior® Star 580 (see Keyresource table). Excitation wavelengths were 561 nm and 640nm respectively and 775 nm STED depletion laser was used. The raw images were then further processed with a Huygens deconvolution software package for STED.

### Electron Tomography and Quantification of LD-Mitochondria Contact Sites

Mice on LFD and mice on HFD for 12 weeks were perfused with 4% PFA in PBS for 8min, via the left ventricle of the heart. The liver was isolated and immediately cut into 2-3 mm small pieces in a dish containing 4% PFA in PBS. Liver pieces were then placed into an immersion fixative (2.5% glutaraldehyde, 2% PFA in 0.1M sodium cacodylate buffer, pH 7.4) for 1-2 hrs. After rinsing in 0.1 M sodium cacodylate buffer, pH 7.4, the tissue was post fixed in 1% osmium tetroxide and en bloc stained in 2% aqueous uranyl acetate for 1hr. Samples were then rinsed and en bloc stained in aqueous 2% uranyl acetate for 1 hr followed by rinsing, dehydrating in an ethanol series and infiltrated with Embed 812 (Electron Microscopy Sciences) resin and baked over night at 60°C. Hardened blocks were cut using a Leica UltraCut UC7. Sections (60nm) were collected on formvar/carbon-coated nickel grids and contrast stained with 2% uranyl acetate and lead citrate. They were viewed using an FEI Tencai Biotwin TEM at 80Kv. Images were taken on a Morada CCD using iTEM (Olympus) software.

LD-mitochondrial contact sites were quantified by counting all mitochondria in an area of 2 μm around the center of each LD. The shortest distance of all mitochondria in this area to the LD surface was measured. Distances that were smaller than 50 nm were considered as contact sites. The percentage of mitochondria in this area in contact with LDs was calculated for the LFD and HFD conditions.

### Protein- and phosphopeptide correlation profiling

For each experiment one mouse liver was used. Protein correlation profiling was performed in three biological replicates and phosphopeptide correlation profiling in 4 biological replicates. PBS perfused livers were isolated and homogenized with a tissue homogenizer on ice in 2.5ml of buffer (20% sucrose, 20mM Tris pH 7.4, 0.5mM EDTA, 5mM KCl, 3mM $MgCl_2$, protease inhibitor and

phosphatase inhibitor cocktail (Roche). 500µl of lysate was kept for the analysis of the total liver proteome and phosphoproteome. The remaining 2ml of liver lysate was centrifuged at 500xg for 15min to pellet nuclei. The nuclear pellet was analyzed as fraction 22 (FR22) in the experiment. 2ml supernatant was loaded onto the top of a continuous 11ml 20%-55% sucrose gradient in 20mM Tris pH 7.4, 0.5mM EDTA, 5mM KCl, 3mM $MgCl_2$, protease inhibitor and phosphatase inhibitor. The subcellular organelles were separated by sucrose-density centrifugation at 100.000xg (Beckmann, Rotor SW41 Ti), for 3hrs at 4°C. To isolate LDs, the 1ml top fraction (FR1) was isolated using a tube-slicer (Beckman coulter). The remaining gradient fractions were subsequently collected with a pipette from the top to the bottom of the gradient (FR2-FR5: 1ml and FR6-FR21: 0.5ml). In total, from each biological replicate and each condition 22 fractions were collected for proteomic and phosphoproteomic analysis.

### *In Vitro* Assay for Golgi Apparatus Targeting

LDs (200µg of protein) purified by sucrose density centrifugation were incubated with 500µg McArdle cell lysate for 1hr at 37°C in a total volume if 1ml buffer containing 200mM Tris pH 7.4, 0.5mM EDTA, 5mM KCl, 3mM $MgCl_2$, protease inhibitor and phosphatase inhibitor cocktail (Roche). Cells were transfected 48hrs before the experiment with mDsRed-Golgi-7 (Addgene plasmid #55832 from Michael Davidson) using Viromer Red (Lipocalyx) and homogenized in the same buffer. After the incubation LD were floated at 150,000xg for 15min at 4°C. The LD fraction was collected with a tube slicer (Beckman). The amount of DsRed was quantified in the LD fraction and as control in the underlying soluble fraction by MS. The experiment was performed in 3-4 biological replicates.

### Sample preparation for proteomic analysis

4× volumes of ethanol/50 mM sodium acetate, pH5.0 were added to each protein sample harvested from the sucrose density gradient. The samples were incubated overnight at room temperature, and the precipitates were recovered by centrifugation at 13,000xg for 15 min at room temperature. Protein pellets were solubilized in lysis buffer (6M guanidinium chloride (GdmCl), 100 mM Tris pH 8.5, 10 mM tris-(2-carboxyethyl)-phosphin-hydrochlorid (TCEP), 40 mM 2-chloroacetamide(CAA)), heated for 5 min at 95°C, and sonicated (Branson probe sonifier output 3-4, 50% duty cycle, 3× 30 s). The protein concentration was determined by a tryptophan assay and adjusted to a concentration of 1 µg/µl. For each fraction 25 µg of protein solution was diluted with 75 µl 15% aqueous acetonitrile (ACN), and digested with 1:50 (protein:enzyme) LysC at 37°C for 3 hrs. Then, 10% aqueous ACN in 25 mM Tris (pH 8.5) was added to obtain a final concentration of 0.5 M GdmCl and a final volume of 300 µl. Samples were incubated with trypsin 1:50 (protein:enzyme) overnight at 37°C.

For the secretome analysis, 100 µl of the collected cell culture supernatant were diluted with 100 µl of 2x TFE digestion buffer containing 20mm TCEP, 80mM CAA, 200mM ammonium bicarbonate (ABC) and 20% (v/v) 2,2,2-Trifluorethanol (TFE), heated for 5 min at 95°C, sonicated (Branson probe sonifier output 3-4, 50% duty cycle, 10× 15 s) and digested with LysC and trypsin 1:50 (protein:enzyme) over night at 37°C.

For all proteomic analyses the digested peptides were acidified to a final concentration of 1% TFA. The peptide solution was cleared by centrifugation and loaded onto activated (30% methanol, 1% TFA) double layer styrenedivinylbenzene–reversed phase sulfonated STAGE tips (SDB-RPS; 3 M Empore) (Kulak et al., 2014). The STAGE tips were first washed with 200 µl 0.2% TFA, then with 200 µl 0.2% TFA and 5% ACN. The peptides were eluted with 60 µl SDB-RPS elution buffer (80% ACN, 5% $NH_4OH$) for single shot analysis of the subcellular organelle fractions and secretome. For the deep proteome analysis of the total liver lysate, peptides were eluted from STAGE tips in three steps (buffer1: 100 mM $NH_4HCO_2$, 40% ACN, 0.5% formic acid, buffer2: 150 mM $NH_4HCO_2$, 60% ACN, 0.5% formic acid, buffer3: 80% ACN, 5% $NH_4OH$). Samples were concentrated in a SpeedVac for 40 min at 45°C and dissolved in 12 µl MS loading buffer (2% ACN, 0.1% TFA).

### EasyPhos

Proteins were precipitated with ethanol/50mM sodiumacetate pH 5.0 overnight at RT and phosphopeptides were enriched using the EasyPhos workflow (Humphrey et al., 2015). In brief, the protein pellets containing ~1mg of protein for the total liver phosphoproteome and ~250µg-1mg for organelle fractions were solubilized in 250µl TFE digestion buffer containing 10mm TCEP, 40mM CAA, 100mM ABC and 10% TFE, under sonication. Proteins were digested with 1:50 (protein:enzyme) trypsin and LysC overnight at 37°C. 75µl of a buffer X (3.2M KCl, 27.5µl 75mM $KH_2PO_4$), 400µl ACN and 47.5µl TFA were subsequently added to the digested peptides, mixed at room temperature for 1 min at 2,000 rpm, cleared by centrifugation and transferred to new Eppendorf tubes. For the enrichment of phosphopeptides, $TiO_2$ beads resuspended in 80% ACN with 6% TFA were added (10:1 beads/protein ratio), and incubated at 40°C for 5min at 2,000 rpm. Afterwards, the beads were pelleted by centrifugation for 1min at 3,500xg, and the supernatant was discarded. Next, beads were washed 4x in wash buffer (60% ACN, 1% TFA) and transferred to new tubes. Then, beads were resuspended in 100µl transfer buffer (80% ACN, 0.5% acetic acid), transferred onto the top of a C8 STAGETip and centrifuged for 5 min at 500xg. Phosphopeptides were eluted with 60µl elution buffer (40% ACN, 15% $NH_4OH$), and collected by centrifugation into PCR tubes. Eluted peptides were concentrated in a SpeedVac for15 min at 45°C and acidified by the addition of 10µl 10% TFA. Phosphopeptides were desalted by SDBRPS stage tipping. For LC-MS/MS analysis peptides were resuspended in 7µl MS loading buffer (2% ACN, 0.1% TFA).

### MS Analysis

For MS analysis peptides were loaded onto a 50-cm column with a 75μM inner diameter, packed in-house with 1.9μM C18 ReproSil particles (Dr. Maisch GmbH) at 60°C. The peptides were separated by reversed-phase chromatography using a binary buffer system consisting of 0.1% formic acid (buffer A) and 80% ACN in 0.1% formic acid (buffer B).

For the analysis of the PCP fractions 2μg of peptides of each organelle fraction was separated on a 120min gradient (5-30% buffer B over 95min, 30-60% buffer B over 5min). For deep proteome analysis of total liver lysate 2μg of peptides was separated on a 240min gradient (2-5% buffer B over 5min, 5–35% buffer B over 190min, 35–60% buffer B over 25min) at a flowrate of 250nl on an EASY-nLC 1000 system (Thermo Fisher Scientific).

MS data were acquired using a data dependent top-15 method with maximum injection time of 20ms, a scan range of 300–1650Th, and an AGC target of 3e6. Sequencing was performed via higher energy collisional dissociation fragmentation with a target value of 1e5, and a window of 1.4Th. Survey scans were acquired at a resolution of 120,000. Resolution for HCD spectra was set to 15,000 with maximum ion injection time of 55ms and an underfill ratio of either 20% or 40%. Dynamic exclusion was set to 20s.

For secretome analysis, 2μg of peptides was separated on a 60min gradient (8-35% buffer B over 45min, 35-60% buffer B over 5min) at a flow rate of 300nl/min on an EASY-nLC1200 system. The maximum injection time was 56ms, at a scan range of 300–1650Th, and an AGC target of 3e6. Sequencing was performed via higher energy collisional dissociation fragmentation with a target value of 1e5, and a window of 1.6Th. Survey scans were acquired at a resolution of 60,000. Resolution for HCD spectra was set to 15,000 with a maximum ion injection time of 56ms and an underfill ratio of 0.1%. Dynamic exclusion was set to 15s.

Phosphopeptides were eluted with a 140min gradient (5–20% buffer B over 85min, 20–40% buffer B over 45min, 40-65% buffer B over 10min) at a flow rate of 300nl/min on an EASY-nLC 1200 system. The maximum injection time was 20ms, at a scan range of 300–1650Th and an AGC target of 3e6. Sequencing was performed via higher energy collisional dissociation fragmentation with a target value of 1e5, and a window of 1.6Th. Survey scans were acquired at a resolution of 60,000. Resolution for HCD spectra was set to 15,000 with a maximum ion injection time of 120ms, and an underfill ratio of 40%. Dynamic exclusion was set to 40s, and apex trigger (4 to 7s) was enabled.

### PRM Analyses

PRM analyses were performed on a Quadrupole-Orbitrap instrument (Q Exactive HF-X). The PRM scan mode consisted of one full scan (resolution of 60,000 at m/z= 200, AGC target= 3e6, maximum injection time= 20ms, scan range= 300-1650m/z) and sequential PRM scans (resolution of 30,000 at m/z= 200, AGC target= 2e5, maximum injection time= 70ms, isolation window= 1.4 m/z, isolation offset= 0.4m/z, NCE= 27, scan range starting from m/z= 100), in which three peptides of the proteins GOLGA2, GOLGA5, VPS13C and PLIN2 were targeted (see Table S7 for peptide sequence information). The retention times of the selected precursors were extracted from a data-dependent acquisition (DDA) discovery run, consisting of one full scan (resolution of 60,000 at m/z= 200, AGC target= 3e6, maximum injection time= 20ms, scan range= 300-1650m/z) and a sequential fragmentation of the twelve most abundant precursors (Top12, resolution of 15,000 at m/z 200, AGC target= 1e5, injection time= 60ms, isolation window= 1.4 m/z, scan range= 200-2000m/z, first fixed mass= 100m/z, NCE= 27). The chromatographic setup was identical for both DDA and PRM methods (same LC system and same column) and the retention time windows for the selected precursors were of 2 minutes.

Extraction of fragment ion chromatograms (integrated peak areas) was performed in Skyline (version 4.1.0.11796 (64-bit)). The transition settings were as follows: ion charges: 1,2; ion types, y, b, p; product ion selection from m/z> precursor to 6 ions. Protein quantities were calculated as the median of the integrated fragment ion peak areas (total area) of two to three peptides for five selected target proteins.

## QUANTIFICATION AND STATISTICAL ANALYSIS

### Data Analysis

Raw mass spectrometry data were processed with MaxQuant version 1.5.1.6 using default setting if not stated otherwise. False-discovery rate (FDR) at the protein, peptide and modification level was set to 0.01. Oxidized methionine (M) and acetylation (protein N-term) were selected as variable modifications, and carbamidomethyl (C) as fixed modification. For analysis of phosphosites, phospho(STY) was added as variable modification. Three missed cleavages for protein analysis and five for phosphorylation analysis were allowed. Label free quantitation (LFQ) and "Match between runs" were enabled. Proteins and peptides were identified with a target-decoy approach in revert mode, using the Andromeda search engine integrated into the MaxQuant environment. Searches were performed against the mouse UniProt FASTA database (September 2014) containing 51,210 entries. Quantification of peptides and proteins was performed by MaxQuant. Bioinformatics analysis was performed with Perseus 1.5.6.2 and Microsoft Excel. Annotations were extracted from UniProtKB, Gene Ontology (GO), and the Kyoto Encyclopedia of Genes and Genomes (KEGG).

### Proteome Analysis

For proteome analysis quantified proteins were filtered for at least three valid values among three biological replicates in at least one of the conditions (LFD, HFD3, HFD12). Missing values were imputed from a normal distribution with a downshift of X and a width of Y. Significantly up-or-downregulated proteins between the three conditions were determined by ANOVA (FDR 0.05). Hierarchical clustering, 1D annotation enrichment, and Fisher's exact test were performed in Perseus.

### Phosphoproteome Analysis

To normalize for differences in protein input, the intensity dependent normalization algorithm in the Perseus software was used. The normalized peptides were filtered for at least 2 valid values among three biological replicates in at least one of the conditions (LFD, HFD3, HFD12). Missing values were imputed. To eliminate the influence of altered absolute protein levels among the different conditions, phosphopeptides in each sample were normalized to the median intensities of each sample. Phosphopeptide with no protein information were discarded from the analysis. Significantly up-or-downregulated phosphosites between LFD and HFD12 were determined by Student's t-test (two sided, FDR 0.1).

### Secretome Analysis

For the secretome analysis quantified proteins were filtered for at least three valid values among four biological replicates in at least one of the conditions (LFD, HFD3, HFD12). Missing values were imputed and significantly up-or-downregulated proteins were determined by Student's t-test (two-sided), FDR 0.05). 1D annotation enrichment and histograms were generated in Perseus.

### Generation of Protein and Phosphopeptide Profiles

In order to normalize for differences in protein input in the organelle fractions, the intensities of phosphopeptides were divided by the total sum of intensities in each sample. For protein profiles the LFQ values were used. Those values represent values already normalized for protein input. To generate the protein and phosphopeptide profiles, the intensities for each identified protein or phosphopeptide were scaled from 0-1. Thereby each identified proteins or phosphopeptide has a value from 0-1 in each of the organelle fractions. To the fraction with the maximum intensity the value of 1 was assigned whereas fractions in which the protein or phosphopeptide was not quantified were set to 0. By plotting those 0-1 scaled intensities over all fractions profiles were generated that are independent of protein levels and just represent the distribution between organelle fractions. For the generation of median protein and phosphopeptide profiles of the biological replicates, intensities of each fraction of all biological replicates from one condition were summed before scaling those summed intensities from 0-1.

### Organelle Assignments

#### *Identification of Separable Compartments and Organelle Markers*

In order to identify the cellular compartments that can clearly be separated by our PCP approach, protein or phosphopeptide profiles (medians from biological replicates) of the proteins and phosphopeptides identified in all three conditions (LFD, HFD3, HFD12) were used for Euclidian hierarchical clustering with average linkage, as implemented in Perseus. This revealed clusters of proteins or phopshopeptides corresponding to distinct subcellular compartments. For these compartments, we then compiled a list of 2199 marker proteins or 4130 phosophopeptides, respectively. Markers were chosen based on their documented GO-annotations and stable cluster assignment among all experimental conditions (selected marker proteins and phophopeptides are indicated in Tables S3 and S4). Due to overlapping and not validated annotations in the database, a marker selection exclusively based on GO-annotations was not useful. Proteins that are subunits of major cytosolic protein complexes and proteins involved in RNA binding translational complexes, whose position in the gradient overlays with organelle clusters, are indicated in Table S3. For HFD12 Golgi apparatus and LD compartment were combined into one category, as they were not separable under this condition.

#### *SVM-Based Assignment of the Main Organelle*

The defined marker set was used for parameter optimization and training of our SVM based supervised learning approach implemented in Perseus software (Deeb et al., 2015). Parameters were set to Sigma=0.2 and C=4. With SVM classification the main subcellular localization was assigned to every identified protein for each condition separately, or for all conditions combined (indicated in Tables S3 and S4). For every protein SVM classification was performed on all fractions of all biological replicates combined. The typical prediction accuracy for marker proteins was around95%, and 90% for marker phosphopeptides.

#### *Assignment of a Secondary Organellar Localization by Correlation Analysis*

As most proteins shown dual subcellular localizations, we implemented an algorithm for correlation analysis in Perseus software to estimate a second subcellular compartment contribution. This algorithm determines the highest correlation between the protein or phosphopeptide profile determined by our PCP experiment with in silico generated combination profiles (the main organelle profile determined in the previous SVM analysis combined with every other possible median organelle marker profile). The correlation value between the experimentally determined protein or phosphopeptide profile and the assigned in silico generated combination profile is given in the output table Tables S3 and S4, and is a measure for the quality of secondary organelle assignment. A quality filter (correlation >0.4) was applied to discard unreliable assignments. The alpha value (0-1) is a quantitative measure for the second organelle contribution.

#### *Correlation- Based Outlier Test*

Proteins significantly changing their subcellular localization between the LFD condition and the HFD conditions were identified by a correlation based outlier test. The analysis was performed pairwise between the HFD3 or HFD12 vs LFD control. In a first step proteins were quality filtered, retaining only proteins with at least two reproducible profiles among all three biological replicates for both compared conditions. Pearson correlations of the profiles of all three biological replicates for both compared conditions were calculated. Only proteins with a maximal Pearson correlation >0.5 between the top2 profiles for both compared conditions were kept for further analysis. In the next step the best two correlated profiles were selected for each protein for both conditions. For those top2 profiles the profile correlations were calculated for both conditions and averaged (MeanCorr(within same conditions)). Then the

average correlations of the biological replicates between the different conditions were calculated (MeanCorr(between conditions)). Proteins reproducibility changing between both conditions were determined based on the difference of both correlation values: dCorr= MeanCorr(between conditions)-MeanCorr(within same conditions). The calculations were performed for Pearson as well as Spearman correlations. Proteins were then sorted from highest (likely hit) to lowest dCorr (likely not changing). For each of the comparisons (early and late time points vs LFD) Hits from Spearman and Pearson correlations were combined for each condition and a combined FDR was calculated. The threshold of the dCorr value was set to 0.28 for both comparisons resulting in a combined FDR 0.2.

To increase the sensitivity for the detection of proteins relocalizing to or from LDs (those affect only one fraction of the protein profile therefore, the relocalization has less impact on the total profile correlation value), we separately identified significantly relocalized LD proteins as those with a significant change of protein abundance (0-1 scaled LFQ intensity) in the LD fraction (FR1) (Student's t-test FDR 0.2), using the set of proteins with reproducible profiles for both time points of HFD compared to LFD.

#### *Identification of Phosphopeptides Associates with Protein Relocalization*

Organelle specific protein phosphorylation that correlates with protein relocalization was identified by applying three subsequent filtering steps. First, among the 16,087 phosphopeptides whose subcellular localization was mapped by PCP, phosphosites significantly changed in the total phosphoproteome analysis were selected (Student's t-test FDR 0.1). From those 1084 phosphosites, 240 localized to proteins with reproducible and robust profile changes identified by the outlier test, or proteins changing their LD localization.

### Filtering of LD Proteins

To identify proteins reproducibly localizing to LDs in any of the three conditions we filtered for proteins with the characteristic "LD peak" (a peak in low density fraction FR1, followed by a strong profile drop in FR2) in all protein profiles of all biological replicates in all three conditions. All 0-1 scaled protein profiles were filtered for the following criteria: criteria1: normalized intensity FR1>0.5 times normalized intensity FR2; criteria 2: normalized intensity FR1>0.3. Hierarchical clustering on the median normalized LFQ intensities of FR1, and Fisher's exact test of GO-term enrichments were performed in Perseus.

### Analysis of Changes of Organelle Proteomes

To define the core organelle proteomes and their changes during HFD of mitochondria, plasma membrane, ER, endosomes, lysosomes, cytoplasm, peroxisome and the nucleus, we filtered proteins for their main organelle assignment by SVMs based on all conditions (Table S6) and calculated an "organelle peak sum" reflecting the extend of organelle localization by summing the PCP values of the main peak fractions of the median organelle profile (main peak fraction was defined as PCP value in this fraction >0.7 in the median profile of all conditions). This "organelle peak sum" is an indicator for the localization of the protein to its main assigned organelle.

## DATA AND SOFTWARE AVAILABILITY

### Data Resources

The mass spectrometry-based proteomics data have been deposited at the ProteomeXchange Consortium (Vizcaino et al., 2014) (http://proteomecentral.proteomexchange.org) via the PRIDE partner repository, with the dataset identifier PXD007653 and password DoYsjWv1.

Normalized median proteins, phosphopeptides and organelle marker profiles were uploaded in our profile database (http://nafld-organellemap.org) and can be plotted and overlaid.